SIGNALS: I. Survey Description

L. Rousseau-Nepton, R P Martin, Cédric Robert Robert, L. Drissen, P. Amram, S. Prunet, T. Martin, I. Moumen, A. Adamo, A. Alarie, et al.

Monthly Notices
of the
ROYAL ASTRONOMICAL SOCIETY

MNRAS **489,** 5530–5546 (2019)
Advance Access publication 2019 September 20

doi:10.1093/mnras/stz2455

SIGNALS: I. Survey description

L. Rousseau-Nepton,[1,2★] R. P. Martin,[2] C. Robert,[1,2,3] L. Drissen,[1,2,3] P. Amram,[4] S. Prunet,[1] T. Martin,[3] I. Moumen,[1,3] A. Adamo,[5] A. Alarie,[3,6] P. Barmby,[7] A. Boselli,[4] F. Bresolin,[8] M. Bureau,[9] L. Chemin,[10] R. C. Fernandes,[11] F. Combes,[12,13] C. Crowder,[1] L. Della Bruna,[5] S. Duarte Puertas,[14] F. Egusa,[15] B. Epinat,[4] V. F. Ksoll,[16] M. Girard,[17] V. Gómez Llanos,[18] D. Gouliermis,[16,19] K. Grasha,[20,21] C. Higgs,[22,23] J. Hlavacek-Larrondo,[24] I.-T. Ho,[19] J. Iglesias-Páramo,[14,25] G. Joncas,[3] Z. S. Kam,[26,27] P. Karera,[3] R. C. Kennicutt,[28] R. S. Klessen,[16] S. Lianou,[7,29] L. Liu,[9] Q. Liu,[30] A. Luiz de Amorim,[11] J. D. Lyman,[31] H. Martel,[3] B. Mazzilli-Ciraulo,[12,13] A. F. McLeod,[32,33] A-L. Melchior,[12] I. Millan,[34] M. Mollá,[34] R. Momose,[35,36] C. Morisset,[18] H.-A. Pan,[37] A. K. Pati,[38] A. Pellerin,[39] E. Pellegrini,[16] I. Pérez,[40,41] A. Petric,[1,42] H. Plana,[43] D. Rahner,[16] T. Ruiz Lara,[44,45] L. Sánchez-Menguiano,[44] K. Spekkens,[46] G. Stasińska,[47] M. Takamiya,[2] N. Vale Asari[11,48,49] and J. M. Vílchez[14]

Affiliations are listed at the end of the paper

Accepted 2019 August 26. Received 2019 August 22; in original form 2018 November 14

ABSTRACT

SIGNALS, the Star formation, Ionized Gas, and Nebular Abundances Legacy Survey, is a large observing programme designed to investigate massive star formation and H II regions in a sample of local extended galaxies. The programme will use the imaging Fourier transform spectrograph SITELLE at the Canada–France–Hawaii Telescope. Over 355 h (54.7 nights) have been allocated beginning in fall 2018 for eight consecutive semesters. Once completed, SIGNALS will provide a statistically reliable laboratory to investigate massive star formation, including over 50 000 resolved H II regions: the largest, most complete, and homogeneous data base of spectroscopically and spatially resolved extragalactic H II regions ever assembled. For each field observed, three datacubes covering the spectral bands of the filters SN1 (363–386 nm), SN2 (482–513 nm), and SN3 (647–685 nm) are gathered. The spectral resolution selected for each spectral band is 1000, 1000, and 5000, respectively. As defined, the project sample will facilitate the study of small-scale nebular physics and many other phenomena linked to star formation at a mean spatial resolution of ∼20 pc. This survey also has considerable legacy value for additional topics, including planetary nebulae, diffuse ionized gas, and supernova remnants. The purpose of this paper is to present a general outlook of the survey, notably the observing strategy, galaxy sample, and science requirements.

Key words: surveys – H II regions – galaxies: star formation.

1 INTRODUCTION

Over the past few decades, the astronomical community has expressed a need for integral field spectroscopy. Multiple instruments (i.e. Integral Field Spectrograph (IFS), Imaging Fourier Transform Spectrograph (IFTS), and Fabry–Perot) have been implemented for this purpose in the visible/near-infrared, most notably the Spectroscopic Areal Unit for Research on Optical Nebulae (Bacon et al. 2001), Fabry–Perot instruments at the Observatoire de Haute-Provence (Garrido et al. 2002) and the Observatoire du Mont-Mégantic (Hernandez et al. 2003), the Infrared Spectrograph on

★ E-mail: r-nepton@cfht.hawaii.edu

the *Spitzer Space Telescope* (Houck et al. 2004), the Potsdam Multi-Aperture Spectrophotometer – Fiber Package (Roth et al. 2005), the Visible Integral-Field Replicable Unit Spectrograph prototype (VIRUS-P; Hill et al. 2008), the Multi-Unit Spectroscopic Explorer (MUSE; Laurent et al. 2006; Bacon et al. 2010), the Sydney-AAO Multi-object Integral Field Spectrograph (SAMI; Bryant et al. 2012), the Sloan Digital Sky Survey IV (SDSS-IV; Drory et al. 2015), and the Spectro-Imageur à Transformée de Fourier pour l'Étude en Long et en Large des raies d'Émission (SITELLE; Brousseau et al. 2014; Drissen et al. 2019). Many other instruments with integral field capabilities are currently being developed, e.g. the Sloan Digital Sky Survey V (SDSS-V; Kollmeier et al. 2017). Several galaxy surveys have been conducted using these instruments while mainly focusing on one specific goal: acquiring a deeper understanding of galaxy evolution from detailed studies of the physical and dynamical properties of their components. Examples include ATLAS^{3D}, *Spitzer* Infrared Nearby Galaxies Survey (Daigle et al. 2006), Virgo high-resolution Hα kinematical survey (Chemin et al. 2006), Gassendi Hα survey of spirals (Garrido et al. 2002; Epinat et al. 2008), Calar Alto Legacy Integral Field Area survey (CALIFA; Sánchez et al. 2012), VIRUS-P Exploration of Nearby Galaxies (Blanc et al. 2013), Mapping Nearby Galaxies at Apache Point Observatory (MaNGA; Bundy et al. 2015; Yan & MaNGA Team 2016), SAMI survey (Konstantopoulos et al. 2013), Las Campanas Observatory PrISM Survey (a.k.a. TYPHOON; Poetrodjojo et al. 2019), and Physics at High Angular resolution in Nearby Galaxies (PHANGS, Rosolowsky et al. 2019). In these surveys, star formation, chemical enrichment processes, and the gas and stellar kinematics were targeted. These are crucial ingredients in the interaction between stellar populations and the interstellar medium (ISM), and in driving feedback acting as a self-regulatory mechanism on the evolution of galaxies.

These IFS studies made significant progress in our understanding of star-forming galaxies. However, at a spatial resolution ranging from a parsec to several kiloparsecs, these studies had a limited impact on our knowledge of small-scale physics within galaxies. At higher spatial resolutions, the MUSE Atlas of Disks (MAD; Erroz-Ferrer et al. 2019) is observing local disc galaxies by focusing on their central parts, providing a good sampling of H II regions in high stellar density environments (centre and/or bulge). Additionally, some extensive studies on nearby H II regions (e.g. Sánchez et al. 2007; McLeod et al. 2015; Weilbacher et al. 2015) have paved the way towards a better understanding of the interaction between stars and the different ISM gas phases. Without being exhaustive, we can mention works using mid-infrared and radio observations of the Milky Way (e.g. Tremblin et al. 2014) and the H II Region Discovery Survey (Anderson et al. 2011), narrow-band imaging in the Visible of the LMC (e.g. Magellanic Cloud Emission Line Survey; Smith, Leiton & Pizarro 2000; Pellegrini et al. 2012) and of M31 (e.g. A New Catalog of H II Regions in M31; Azimlu, Marciniak & Barmby 2011), or studies using spectral information with intergral field units (IFU; e.g. with MUSE on NGC 300; Roth et al. 2018). Additionally, the upcoming Local Volume Mapper (LVM) survey will use SDSS-V to cover the Milky Way and other nearby galaxies.

Despite these advancements, the need for spectroscopic surveys with a high spatial resolution on a large number of H II regions remains. We need to study a detailed and uniform H II sample in all galactic environments. Canada–France–Hawaii Telescope (CFHT)'s IFTS SITELLE was intentionally designed for this purpose and is currently the most efficient instrument to conduct such a study. With its large 11 arcmin × 11 arcmin field of view (FOV), SITELLE's spatial coverage is 100 times bigger than any current competitor. Compared to fibre-fed systems, SITELLE gathers a much larger fraction of the light coming into the instrument with much better spatial sampling (0.32 arcsec per pixel) and improved blue sensitivity.

SIGNALS, the Star formation, Ionized Gas, and Nebular Abundances Legacy Survey, is using SITELLE to observe more than 50 000 resolved extragalactic H II regions in a sample of ∼40 nearby galaxies over three spectral ranges (363–386, 482–513, and 647–685 nm). By studying the spatially resolved spectra of individual H II regions and their massive stars content, SIGNALS' main scientific objective focuses on how diverse local environments (nearby stellar population mass and age, dynamic structures, gas density, chemical composition, etc.) affect the star formation process. The legacy of this survey will also contribute to many topics in astrophysics, from stars to very distant galaxies. More specifically, the primary goals of SIGNALS are

(1) to quantify the impact of the surrounding environment on the star formation process;
(2) to link the feedback processes to the small-scale chemical enrichment and dynamics in the surrounding of star-forming regions; and
(3) to measure variations in the resolved star formation rate with respect to indicators used to characterize high-redshift galaxies.

This paper presents an overview of the SIGNALS project observational strategy and data reduction (Section 2), galaxy sample (Section 3), science goal requirements (Section 4), data products (Section 5), and legacy value (Section 6).

2 OBSERVATIONS AND DATA REDUCTION

2.1 Strategy and filter configurations

SITELLE was designed to be optimized for the study of emission line objects. A lot of technical challenges were overcome while building the instrument to assure excellent sensitivity, a high spectral resolution, and a large FOV (Drissen et al. 2019). SIGNALS' observing strategy is built upon SITELLE's unique capabilities. Three filters are used to optimize the detection and characterization of the strong diagnostic lines for nearby extragalactic nebulae: SN1 (363–386 nm) with the [O II]λ3727 and the Balmer emission lines H9 to H12 (detected in bright regions), SN2 (482–513 nm) with Hβ and [O III]λλ4959,5007, and SN3 (647–685 nm) with Hα, [N II]λλ6548,6583, He Iλ6678, and [S II]λλ6717,6731. These filters also provide a sampling of the continuum. Fig. 1 shows an example of the deep images obtained combining the data from the three SIGNALS filters using two different methods for M33. This data set was acquired for the science verification of the SIGNALS project and includes four fields. Fig. 2 shows an example of an H II region spectrum in NGC628 obtained with SITELLE during its commissioning (Rousseau-Nepton et al. 2018). The main lines investigated by the survey are compiled in Table 1. The SITELLE Exposure Time Calculator (ETC) was used to simulate the expected signal-to-noise ratio (SNR) for specific lines and to define the instrumental configurations (i.e. spectral resolution, exposure time, and Moon maximal contribution). The ETC SNR calculation includes both the contributions of the sky and the target emission to the photon noise. The main driver for the configurations' selection was the detection threshold (while avoiding saturation of the detector) over the range in surface brightness (SB) observed in H II regions, from

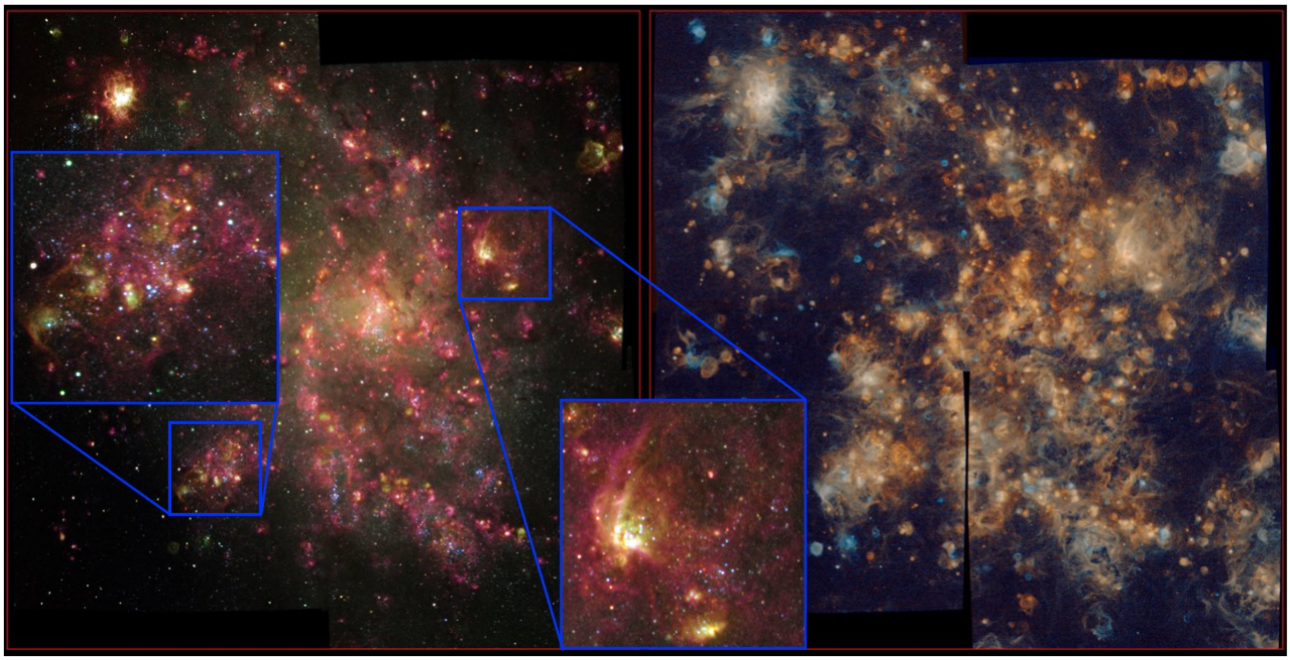

Figure 1. M33: SIGNALS' science verification data (a mosaic of four fields). On the left, a composite image using the three filters. It combines the three continua over the wavelength range of the filters plus one emission line for each: SN3 + Hα (red), SN2 + [O III]λ5007 (green), and SN1 + [O II]λ3727 (blue). The blue squares are zooms in two areas to show additional details. On the right, to emphasize the ionized gas component, we used the emission line map of Hα, [O III]λ5007, and [O II]λ3727 with different shades of orange, green, and blue, respectively.

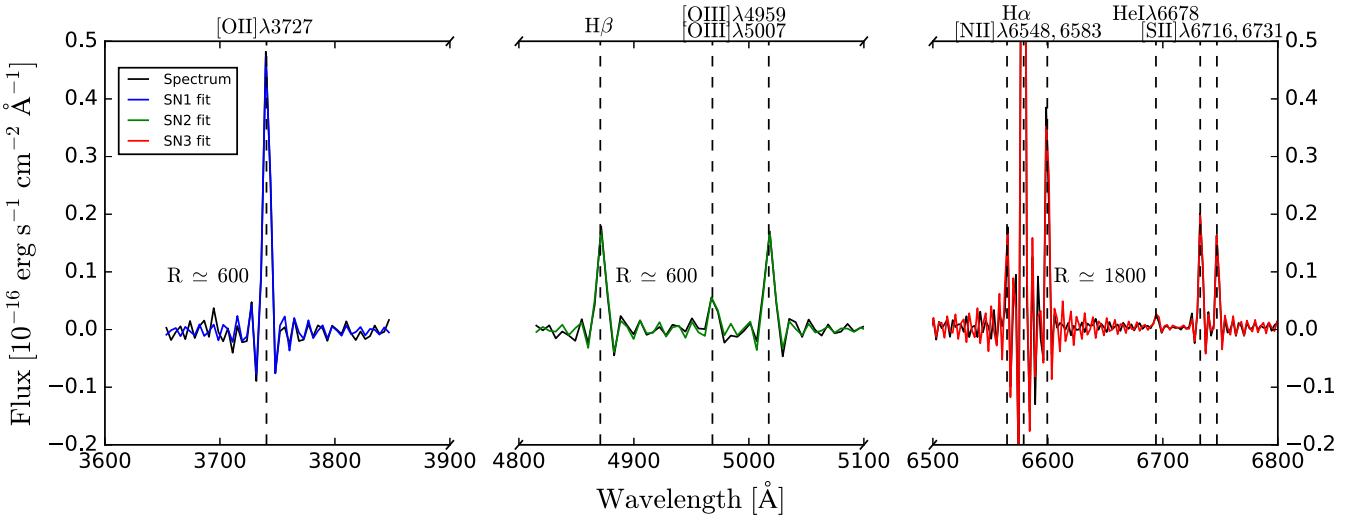

Figure 2. Continuum-subtracted spectrum of an H II region in NGC 628 extracted from the datacubes using a circular aperture with a radius of 1.6 arcsec, centred at RA $01^{h}36^{m}53.1^{s}$ and DEC $+15^{\circ}48'04.8''$. The fits obtained with ORCS (Section 5) for the emission lines are shown. Note that SITELLE's line profiles are fitted using a cardinal sine (sinc) function. Spectral resolutions obtained here are significantly smaller than those selected for SIGNALS.

$\sim 8 \times 10^{-17}$ to 8×10^{-12} erg s^{-1} cm^{-2} arcsec^{-2}. Table 2 summarizes the parameters for the three selected configurations.

The instrumental configuration for SN1 and SN2 was set using a spectral resolution of 1000, enough to separate the emission lines (the unresolved [OII]$\lambda\lambda$3726,3729 doublet; hereafter [OII]λ3727, [OIII]λ4959, [OIII]λ5007, and Hβ) and to properly measure the stellar continua. For the SN3 filter (648–685 nm), which contains the Hα line broadly used to study gas dynamics, we adopted a higher spectral resolution of $R = 5\,000$ in order to reach a precision on the velocity measurements of $\sim$0.1 to 10 km s^{-1} (for H II regions with an SNR of 1000 to 10). With this configuration, we are also sensitive to velocity dispersion ranging from 30 km s^{-1} for a faint region (over one seeing element) down to $\sim$10 km s^{-1} for most of the regions observed and $\sim$1–2 km s^{-1} for the brightest resolved regions. Fig. 3 shows the relation between the minimum measurable broadening ratio of the Gaussian over the sinc functions used to fit a line of a given SNR. Appropriate binning can be used to reach a higher precision on the velocity measurements for kinematic studies (see Section 4.8).

With these configurations, the detection thresholds (SNR > 3) over an element of resolution of 1 arcsec are $SB_{H\alpha} \simeq 3.6 \times 10^{-17}$ erg s^{-1} cm^{-2} arcsec^{-2},

Table 1. Main emission lines for SIGNALS.

Ion	Description
[O II]	[O II]λλ3726,3729
H II	Hβ (4861 Å)
[O III]	[O III]λ4959
[O III]	[O III]λ5007
[N II]	[N II]λ6548
H II	Hα (6563 Å)
[N II]	[N II]λ6583
He I	He Iλ6678
[S II]	[S II]λ6716
[S II]	[S II]λ6731

Table 2. Filter configurations.

Filter	Band (nm)	Spectral resolution	Exposure time (s per step)	Number of steps	Integration time (h)
SN1	363–386	1000	59.0	172	3
SN2	482–513	1000	45.5	219	3
SN3	647–685	5000	13.3	842	4

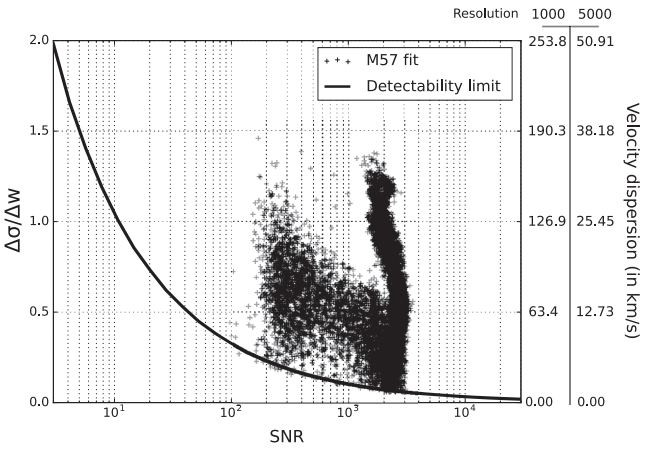

Figure 3. Instrument line spread (ILS) function ratio. The black line shows the minimum measurable ratio $\Delta\sigma$ (observed)/Δw (theoretical or pure sinc) for a line with a given SNR. The corresponding velocity dispersion at the two different resolutions used for SIGNALS (5000 and 1000) is reported on the right axis. It scales linearly with the resolution. A set of points from a fit of NGC6720 data with ORCS (Martin & Drissen 2017) is overlapped to the prediction. In this case, we can see that the SNR of the data points is high because all the lines in each spectrum are fitted with the same broadening parameter.

$SB_{H\beta} \simeq 4.2 \times 10^{-17}$ erg s^{-1} cm^{-2} arcsec^{-2}, and $SB_{[O\,II]3727} \simeq 3.0 \times 10^{-17}$ erg s^{-1} cm^{-2} arcsec^{-2} for SN3, SN2, and SN1, respectively. We used Hα, Hβ, and [O II]λ3727 as reference since they are the key lines of interest in their respective filters. Note that the threshold for Hα corresponds to an SNR of 6.7 on the faintest H II regions and is also good for further investigation of the diffuse ionized gas (DIG; see Section 4.7) component at $SB_{H\alpha DIG} \simeq 5 \times 10^{-18}$ erg s^{-1} cm^{-2} arcsec^{-2}; additional binning may also be used later during the analysis. No extinction was applied on the ETC simulations, but, adopting these numbers, we estimated that over 30 per cent of the pixels detected in Hα will have an Hβ detection before applying any spatial binning. This is also supported by the relative detection we obtained on other galaxies during commissioning of SITELLE. After spatial binning, this detection threshold ensures that most H II regions will have a reliable measurement of the Hα/Hβ ratio on the integrated spectra (>95 per cent; considering a mean extinction $E(B-V) \simeq 0.5$ and no background).

The current average seeing of the fields that have already been observed is 1.0 arcsec. The seeing of the observations is limited to a mean value of 1.2 arcsec over a scan in order to maintain the global spatial sampling of the H II regions. Data observed with a mean seeing greater than 1.2 arcsec are not validated. The Moon contribution must be minimal for the blue SN1 filter. For the other two filters, the Moon contribution can be moderate (50 per cent illumination and at a distance greater than 70°) without affecting the detection threshold significantly.

2.2 Data reduction and calibrations

Two software components have been developed specifically for the reduction and spectral analysis of SITELLE's datacubes: the data reduction software, ORBS, and the data analysis software, ORCS (Martin, Drissen & Joncas 2015; Martin, Prunet & Drissen 2016).

ORBS is a fully automated data reduction pipeline, tailored for IFTS data, transforming the interferogram cube of SITELLE's cameras into a spectral datacube. The first ORBS data processing step includes the wavelength calibration using a He–Ne laser datacube observed during the same observing run as the science datacube. As they come out of the reduction pipeline, datacubes have a pixel-to-pixel velocity error estimated to be of the order of 0.1 km s^{-1} at $R = 5000$. Additional correction is applied to the absolute wavelength calibration using the sky lines' centroid map as described in Martin, Drissen & Melchior (2018) resulting in an accuracy of ∼1 km s^{-1} on the measured relative velocities across the FOV (see appendix B of Martin et al. (2016) for details).

The first data processing also includes a correction of the zero, first, and greater than one phase orders as described in Martin & Drissen (2017). This ensures an ILS function that follows the theoretical model according to the selected instrument configuration. The ILS function for SITELLE is a pure sinc function. The full width at half-maximum (FWHM) of the sinc function is known and fixed since it depends only on the sampling and the maximum optical path displacement of the interferogram scan (Martin et al. 2016; Drissen et al. 2019). As shown in the work of Martin et al. (2016), when natural line broadening is observed, a sinc convolved with a Gaussian function can be used to properly recover the line parameters. If so, the line model has three varying parameters (amplitude, velocity, and broadening of the Gaussian). The uncertainty on the measurements depends on the SNR and the proper selection of the line model (sinc or sinc + Gaussian) and the set of lines to be fitted for each pixel (all lines must be fitted simultaneously, and if multiple components are present, they must be fitted simultaneously as well). As also described in Martin et al. (2018), the precision on the velocity obtained over the planetary nebulae in M31 ranged from 2 to 6 km s^{-1} for sources of SB much lower than what is expected for most H II regions.

The ORBS flux calibration uses flat images and standard star images taken during the same night as the science observation as well as standard star datacubes from the same observation run. The airmass is corrected using the atmospheric extinction curve

above Mauna Kea provided by The Nearby Supernova Factory et al. (2013) and the mean airmass of the cube. Atmospheric extinction variations through a datacube are corrected using the transmission function extracted by normalizing the combined interferogram of the two output detectors to the maximum flux observed through the scan. Since a datacube is observed over a period of 3–4 h and the transmission variations are corrected and normalized to the best transmission conditions seen during this period, the transmission variation is completely negligible. The flux calibration function itself is extracted from the standard star datacube using the star integrated spectrum in a given filter corrected for its own airmass and is used as a reference for the zero-point correction. Zero-point variations are tracked and corrected using the standard images taken during the night in photometric conditions. This data reduction procedure ensures a pixel-to-pixel relative flux calibration accuracy better than 2 per cent. The datacube-to-datacube relative flux calibration accuracy is better than 5 per cent (Martin & Drissen 2017), including both random and systematic errors. This will be improved in the second release of ORBS currently being developed for the SIGNALS programme. Fig. 4 shows the relative overlap between the SITELLE and the SDSS filters. Comparison with ancillary data can always be made to improve the flux calibration before the second data release.

3 SAMPLE OF H II REGIONS

Our sample selection was driven by the need to observe a very large number of extragalactic H II regions in as many different galactic environments as possible. Star-forming areas within galaxies therefore motivated our choice. They were identified from existing Hα and UV-*GALEX* images from all nearby galaxies observable by CFHT. To allow for a minimum contiguous observing period of 2 h from Mauna Kea with an airmass of 1.5 or smaller, targets with a declination below -22° and over $+62^{\circ}$ (i.e. the limits of the instrument) were rejected. The maximum galaxy distance was set to 10 Mpc in order to optimize the spatial resolution while still sampling a large number of H II regions. This ensures a spatial resolution of 40 pc per resolution element or less for a seeing of 0.8 arcsec. Our selection criteria can be summarized as follows:

(1) star-forming galaxies;
(2) $-22^{\circ} <$ Dec. $< +62^{\circ}$;
(3) $D \leq 10$ Mpc;
(4) limited amount of dust on the line of sight; and
(5) limited crowding of the H II regions (inclination $\leq 71^{\circ}$).

Here, crowding refers to observing multiple HII regions along the line of sight.

Based on these criteria, our sample of potential targets includes 54 objects. Except for some very large objects, most targets necessitate only one SITELLE field. As a result of the first criterion, some non-active areas and entire galaxies were rejected. For instance, galaxies such as the Cetus Dwarf Spheroidal and DDO 216, as well as the very outskirts of some extended galaxies (like M33), were excluded if they contained fewer than 10 regions within one pointing in order to increase our observing efficiency. To minimize the effect of internal dust extinction, we excluded massive, dusty, edge-on spirals from the sample (e.g. NGC 4631, NGC 4244, NGC 4605, etc.). However, we kept the foreground portion of the M31 disc. Table A1 contains the list of potential targets for the survey and a summary of their properties. Among this sample, 36 fields will be selected and observed with the SITELLE filters SN1, SN2, and SN3, for a total of 355 h. By extrapolating from available Hα images of the galaxies, the number of fields observed, and the known accuracy of the region identification as a function of spatial sampling, we estimate that about 50 000 H II regions will be analysed. Each semester, an updated list will be published on the SIGNALS website.[1]

Other selection criteria should also guarantee the uniformity of the sampling of different galactic environments: the oxygen abundance $12 + \log[\mathrm{O/H}]$, varying from 7.5 in Sextans A (Kniazev et al. 2005) to $\geq$9.0 in objects like M51 and M63 (Pilyugin, Contini & Vílchez 2004); the stellar density (proportional to μ_{V}), ranging from μ_{V} below 30 mag arcsec^{-2} up to 18 mag arcsec^{-2}; the molecular and neutral gas mass, which is also very different between these galaxies; and galactic structures (size of the bulge, spiral arms, bars, rings, faint external structures, etc.). The objects selected are broadly distributed in mass with the addition of smaller irregular galaxies in order to sample different metallicities and environments with a similar statistical weight. The Hubble-type and distance distribution of the sample is shown in Fig. 5. The properties that were important for the completion of our sample can be summarized as follows:

(1) global metallicity: $7.5 \lesssim 12 + \log[\mathrm{O/H}] \lesssim 9.0$;
(2) magnitude: $-21.3 \lesssim M_{\mathrm{absolute}} \lesssim -13.5$ mag;
(3) SB: 18 mag arcsec$^{-2} \lesssim \mu_{\mathrm{V}} \lesssim 30$ mag arcsec^{-2}; and
(4) galactic environments: 1/3 isolated objects and 2/3 in groups, with no strongly interacting systems.

The group property of the galaxies was extracted from the NASA/IPAC Extragalactic Database (NED).[2]

As the data are analysed, the selection can be adjusted to properly sample the different environments. For example, if we gather enough high-metallicity and dense environment regions, we will then concentrate on the small irregular galaxies with a low metallicity. We will prioritize the completion of the science goals and that depends mostly on the sample of H II regions and less on the completion of one particular target.

Among SIGNALS' galaxy sample, seven targets are very close, resulting in a spatial resolution below 3 pc in the best observing conditions. A mosaic of several fields with small overlaps is used for these objects to cover most of the star formation activity. Fig. 1 shows an assemblage of four fields in M33 from the SIGNALS pilot project obtained in 2017. Reaching such a high spatial resolution is essential for some objectives of the project, i.e. to resolve gas ionization structures and the ionizing star content of the nebulae (e.g. faint end of the H II region luminosity function, calibration of the models with resolved structure of ionized gas, etc.).

The spatial resolution of the sample ranges from 2 to 40 pc. It should complement the MUSE survey over the northern sky (PHANGS/MUSE). Out of 19 galaxies, SIGNALS has 6 in common with PHANGS/MUSE. We also compiled existing data from *HST* + Legacy ExtraGalactic UV Survey (LEGUS) (28 galaxies), *GALEX* (UV, 39 galaxies), *Spitzer* (IR, 43 galaxies), BIMA and ALMA (CO, 23 galaxies), and VLA (HI, 42 galaxies), as well as those obtained with narrow-band filters. These will be used to complete

[1] http://www.signal-survey.org
[2] The NED is operated by the Jet Propulsion Laboratory, California Institute of Technology, under contract with the National Aeronautics and Space Administration.

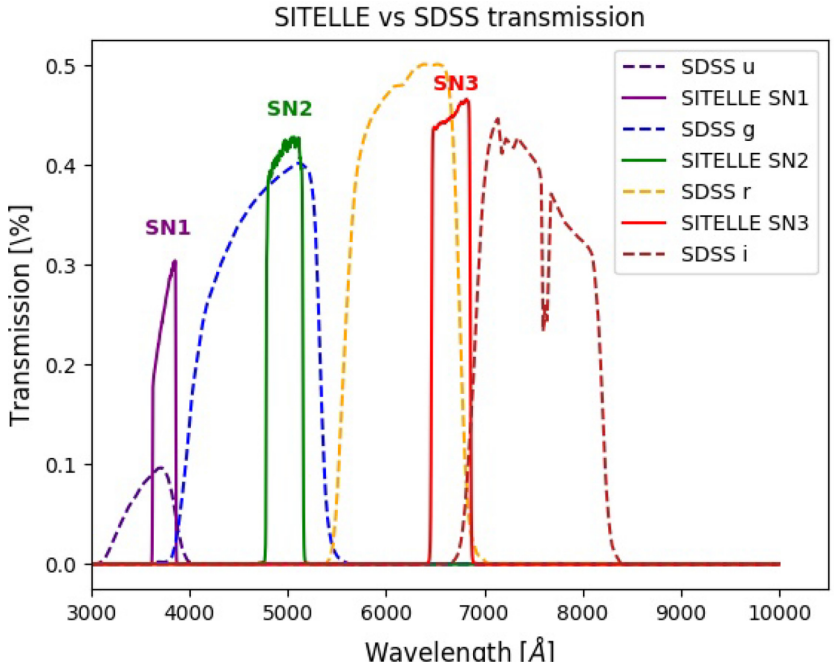

Figure 4. Transmittance curves for the atmospheric (airmass = 1), telescope, and optical assembly from SITELLE and SDSS. The SIGNALS filters (SN1, SN2, and SN3) are shown along with the overlapping SDSS filters.

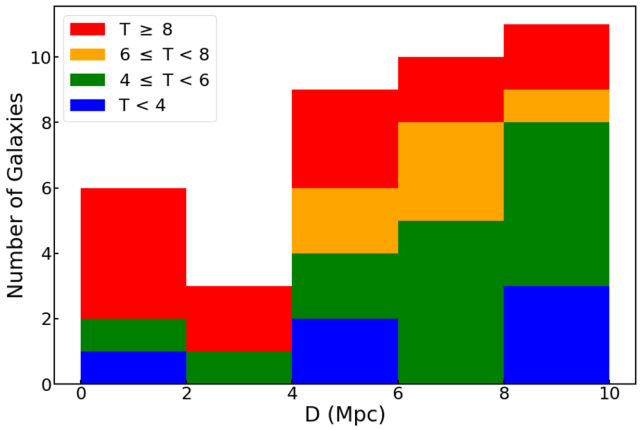

Figure 5. Distribution of the primary targets as a function of distance. The galaxies are colour coded according to their morphological type, as given by the parameter *T* from the revised Hubble classification scheme.

our analysis. The availability of these complementary data for the SIGNALS sample is also indicated in Table A1.

4 SCIENCE REQUIREMENTS

SIGNALS aims to measure the strong emission lines while resolving individual H II regions. We also want to measure the Hα brightness of the DIG, study small-scale dynamics of the gas, and investigate feedback mechanisms at the scale of H II regions. As described in Section 2.1, the observation strategy was defined from basic constraints related to the detection of faint H II regions and the DIG with respect to their expected SB and the known velocity dispersion observed in the ionized gas. The target selection was based on the spatial resolution requirement and the efficiency at observing a large number of H II regions in different local environments.

As described in this section, different steps resulting in the proper measurements of the emission line and continuum fluxes, as well as the velocity and its dispersion, were tested during the design of the survey: (1) an additional wavelength calibration for the velocity field is obtained by fitting the OH sky lines of the SN3 filter subtraction; (2) the sky subtraction is performed using sky sampling through each datacube; and (3) the stellar continuum subtraction is applied pixel by pixel using a model for the stellar population. Finally, once the lines are properly measured, the analysis involves (4) a dust correction using the Balmer decrement method; (5) the identification of emission regions; and (6) characterization using photoionization models. Requirements for meeting science goals on the study of (7) the feedback processes; (8) the dynamics; and (9) the impact of local environments are also introduced in this section.

4.1 Wavelength calibration using sky lines

As mentioned in Section 2.2, the wavelength calibration provided by the data reduction pipeline ORBS is performed by measuring the position of the laser line on a He–Ne datacube through the FOV, and applying the measured centroid map to scale the science cube spectral axis (Martin & Drissen 2017). Some velocity residual errors remain from this technique since the science observations are made at different on-sky positions than those of the calibration laser (zenith). As described in Martin et al. (2016, 2018), the sky lines observed in the SN3 filter can be used to correct residual errors. A simultaneous fit of all the bright sky lines available in the bandpass is made using the ORCS analysis tool. The resulting velocity map is interpolated over the FOV and a correction map is then applied to any subsequent velocity map extracted from the emission line with ORCS. Note that at $R = 5000$, the sky lines are well resolved

and their number reduces the uncertainties on the velocity extracted from the fit. The same accuracy is not required for the SN1 and SN2 filters.

4.2 Sky subtraction

The sky subtraction is performed on each pixel using a high SNR sky spectrum built from each datacube. This sky spectrum is extracted using the median of the available sky spaxels over the FOV. Although a few hundred pixels is enough to produce such a spectrum that corresponds to an area greater than $\sim$10 arcsec^2 on the sky, all the available sky spaxels can be used to produce the median sky spectrum. The selection of those sky spaxels is made from the deep image of the datacube (the deep image is the image produced from the stacked datacube along the spectral axis) by defining a maximum threshold on the image intensity. This threshold can be adjusted from one target to another to optimize the selection of the faintest pixels while still using a large number of them. This adjustment is important to minimize the DIG or stellar background contamination to the sky spectrum. We estimate that the vast majority of all SIGNALS fields will have enough sky sampling to perform the high SNR sky spectrum subtraction (i.e. at least 10 000 sky spaxels corresponding to an SNR $\geq$100). For pointings without any pixels enabling the sampling of the sky, we use a model of the sky spectrum obtained by fitting the bright lines with ORCS. Since the emission of the sky can vary in time and since it includes a faint Hα component, a model is used only when a high SNR sky spectrum cannot be produced.

4.3 Stellar continuum subtraction

The stellar population contribution to each spaxel is subtracted to obtain the proper emission line fluxes. At the SIGNALS spatial resolution of 2–40 pc, the effect of stellar continuum subtraction is much smaller than that at resolution of 1 kpc. The emission of the gas is concentrated in clumpy areas, while the stellar population in massive galaxies is more uniformly distributed. For example, at a $\mu_V = 18$ mag arcsec^{-2}, the intensity of the continuum is 2.65×10^{-17} erg s^{-1} cm^{-2} Å^{-1} arcsec^{-2}, which corresponds to 2.71×10^{-18} erg s^{-1} cm^{-2} Å^{-1} per pixel. Note that this level corresponds closely to the level of noise in one spaxel for any given SIGNALS datacube. For low-mass galaxies, no continuum subtraction is necessary for our project. Nevertheless, the continuum can dominate the emission in the central part of massive galaxies. To properly measure the emission from faint H II regions or the DIG components in those areas ($SB_{H\alpha DIG} \simeq 5 \times 10^{-18}$ erg s^{-1} cm^{-2} arcsec^{-2}), a subtraction of the stellar population background needs to be performed.

As shown in Rousseau-Nepton et al. (2018), a stellar continuum can be extracted directly from the datacubes. At a resolution of $R = 5000$, the stellar absorption line can be fitted along with the emission line. This is important for the Hα and Hβ absorption lines. For the galaxies observed in SIGNALS, the stellar population continuum subtraction will be performed in three steps: (1) a fit of the gas emission will be performed to obtain an estimate of the velocity field, the emission line fluxes, and the continuum level; (2) the aperture for the stellar continuum sample will be defined using the galaxy luminosity profile; and (3) the stellar population spectra will be extracted or fitted through the apertures and used to subtract the component from each spaxel (e.g. Moumen et al. 2019). Ideally, when the SNR and spatial resolution allow it, the local environment will be used to build the galaxy background spectrum directly from the datacubes. While selecting the pixels to build the stellar continuum spectra, a limit on the combined emission line map flux (from a preliminary fit of the emission with ORCS) is used to exclude pixels with a significant contribution from the DIG and/or surrounding H II regions. If no pixel passes this selection test, or if the noise level of the stellar continuum spectrum is higher than 1/10 of the detection threshold for the H II regions, the aperture is increased. Depending on the galaxy, this method will not always be possible and other ones will be considered.

Also discussed in Rousseau-Nepton et al. (2018), although some pixels within an emission region may be affected by the young population continuum flux and absorption lines, our method for the subtraction of a local or global background stellar population spectrum takes into account most of the young population emission. Indeed, when the stellar population spectrum is subtracted, it is first rescaled to the continuum level of the emission region, which takes into account the continuum level of the young population. The absorption line profiles in this rescaled stellar population spectrum do not contain the exact contribution from the young population, but this inaccuracy is negligible compared to the final noise level in the emission lines. Tests done with a combination of model spectra for young and old populations with different ages and proportions support this idea.

4.4 Dust extinction correction

The dust extinction contribution is included in our model for the spectral analysis. To provide dust corrected fluxes, the extinction law of Cardelli, Clayton & Mathis (1989) is used and the colour excess $E(B-V)$ is evaluated from the known equation

$$E(B-V) = \frac{2.5}{1.10} \log \left[\frac{(F_{H\alpha}/F_{H\beta})_{obs}}{(F_{H\alpha}/F_{H\beta})_{theo}} \right], \quad (1)$$

with $(F_{H\alpha}/F_{H\beta})_{theo}$ given by the photoionization models, and $E(H\beta - H\alpha)/E(B-V) = 1.10$.

Measured fluxes, both corrected and uncorrected for the dust extinction, will be provided in the catalogue of H II regions (see Section 5).

4.5 H II region identification

To separate individual H II regions, a spatial resolution of the order of 10 pc is required. Fig. 9 from Kollmeier et al. (2017) illustrates how the ionized gas structures and individual clumps of star formation can be resolved by increasing the spatial resolution. Below a resolution of 50 pc, observations reveal structures in the ISM including individual star-forming knots, DIG, and shocks. The filling fraction of the observations is also important for analysing the gas photoionization conditions. Fig. 6 shows the impact of the FOV and filling factor on the H II region spectrophotometry by comparing the log([N II]λ6583/Hα) maps obtained with SITELLE and the CALIFA PPAK IFU survey (filling factor $\sim$60 per cent; Rosales-Ortega et al. 2011). The maps differ significantly. Notably, the flux of faint areas covered by fibres (for fibre-fed systems) becomes negligible resulting in a total flux per resolution element dominated by the brightest zones. Areas not covered by fibres do not contribute to the resulting map.

Our analysis of the science verification data allowed us to identify 4285 H II region candidates in NGC 628 using a tailored procedure developed for the SITELLE data at a spatial resolution of 35 pc. Details are published in Rousseau-Nepton et al. (2018). There are two advantages of the IFTS that our procedure uses: the full spatial

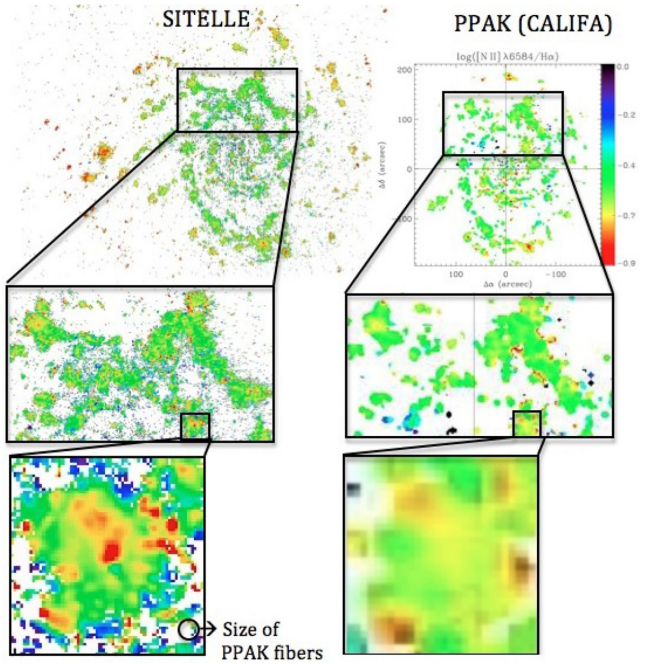

Figure 6. Spatial resolution and filling factor impact on the measurements of emission line ratios. The line ratio log([N II]λ6583/Hα) extracted from SITELLE's observations on NGC 628 (0.8 arcsec seeing, 0.32 arcsec per pixel, 100 per cent filling factor) is compared to PPAK's observations on the same area (0.8 arcsec seeing, 2.7 arcsec per fibre, 60 per cent filling factor). The colour scale is the same for both maps (upper-right corner). The PPAK map (on the right) is published in Rosales-Ortega et al. (2011) and is re-used here for comparison purpose only.

coverage and the spectral information. By combining the flux of three emission lines (Hα, Hβ, and [O III]λ5007), we increased the detection threshold and improved the detection of the low-metallicity regions with much fainter recombination lines. This code provides flexibility in defining the regions and their DIG background. Our method proceeds through multiple steps: (1) the identification of the emission peaks; (2) the determination of the zone of influence around each peak; and (3) the definition of the outer limit of a region and its DIG background. Fig. 7 shows the border of a few H II regions derived from this procedure. For SIGNALS, it will be adapted to different spatial resolutions to make sure that the regions are uniformly defined. SITELLE's data set for NGC 628 was used to recover the luminosity function for different samples of H II regions as shown in Rousseau-Nepton et al. (2018). These luminosity functions, established from 2000–4000 regions, are well sampled and provide interesting insights into the active star formation processes within that galaxy.

4.6 H II region characterization

Photoionization models are usually employed to understand the physical properties of H II regions, whether or not their ionization structure is resolved, e.g. CLOUDY (Ferland et al. 1998; Morisset, Delgado-Inglada & Flores-Fajardo 2015) or MAPPINGS (Dopita & Sutherland 1995; Ho et al. 2014). The ensemble of emission lines listed in Table 1 will allow us to investigate a broad range of physical conditions for the gas and ionizing sources (Kewley & Dopita 2002; Pérez-Montero et al. 2014; Vale Asari et al. 2016). With those lines (and their ratios), we are planning three different modelling strategies for SIGNALS: integrated spectra modelling, spatially resolved modelling, and modelling the populations.

4.6.1 Emission line detection

The intensities of the strong nebular lines vary with the physical conditions in the gas. Nevertheless, we can make some assumptions about the detectability of the strong lines from previous observations and grids of photoionization models. When a line is not detected, the detection threshold adds a constraint on the line's flux that can still be used to narrow down the region's physical conditions. Depending on the region size and the spatial resolution, the detection threshold changes and this effect has to be considered as an observational bias in the subsequent analysis.

For nearby targets, most regions will be spatially resolved and multiple spaxels will be available to increase the detection limit. For the faintest regions, considering an SB of $\sim 8 \times 10^{-17}$ erg s^{-1} cm^{-2} arcsec^{-2} and a radius of 2 arcsec, an SNR of 3 would be reached for any line with a flux greater than 12 per cent of Hα (or log[line/Hα] ≥ -0.9). For any region with an SB greater than 3.4×10^{-16} erg s^{-1} cm^{-2} arcsec^{-2} and a radius of 2 arcsec, an SNR of 3 would be reached for any line with a flux greater than 3 per cent of Hα (or log[line/Hα] ≥ -1.5). According to photoionization models (Vale Asari et al. 2016), this corresponds to virtually all the regions for [N II]λ6583, [S II]λλ6716,6731, and [O II]λ3727. Fig. 8 shows the expected ratios of the strong lines over Hα for a set of models from the Bayesian Oxygen and Nitrogen abundance Determinations data base (BOND; Vale Asari et al. 2016) including models for ages ranging from 1 to 6 Myr, optical depth of 1.0, log[N/O] ranging from 0 to -2.0, 12 + log[O/H] ranging from 6.5 and 9.5, and ionization parameters ranging from -2.5 to -4 (value observed in the CALIFA sample; Morisset et al. 2016). We can see that within the range of metallicity expected for the extragalactic H II regions of the sample, all models show strong lines' relative intensities ≥ -1.5. For [N II]λ6583, we considered only regions with a log[N/O] above -1.5, since H II regions are not observed frequently below that threshold (Berg et al. 2015; Croxall et al. 2015, 2016). It is important to note that for [O III]λ5007, some cases will not be detected, i.e. regions older than 5 Myr or with a low ionization parameter (≤ -3.5). Note that in both cases the regions are fainter compared to others since the ionizing photons come from late B star(s). Nevertheless, not detecting the [O III]λ5007 line is a good constraint for the models. From the whole sample of spatially resolved H II regions (2–15 pc), a good fraction of them will have strong emission lines detected along the region profile, useful for our detailed 2D analysis (see Section 4.6.3).

For further-away targets, we can approximately estimate the number of regions for which we will detect strong emission lines by comparing model predictions with observations. Two parameters mainly influence the detection of emission lines for unresolved regions: the size distribution of the regions with respect to the resolution of the data and the SB distribution of regions with respect to their size. Some small and faint regions cannot be detected in targets near the distance limit of the SIGNALS sample. Their flux is diluted in the resolution element. In the commissioning data of NGC 628, located at 9 Mpc, our measured detection threshold for Hα was 4.6×10^{-17} erg s^{-1} cm^{-2} arcsec^{-2} (slightly lower than that for SIGNALS). Fig. 9 shows the measured peaks' SB function (histogram of the SB of the central pixel) of the regions detected with the identification procedure (Rousseau-Nepton et al. 2018) for different subsets of regions on NGC 628 for which there is a detection of a different strong line. From the regions detected

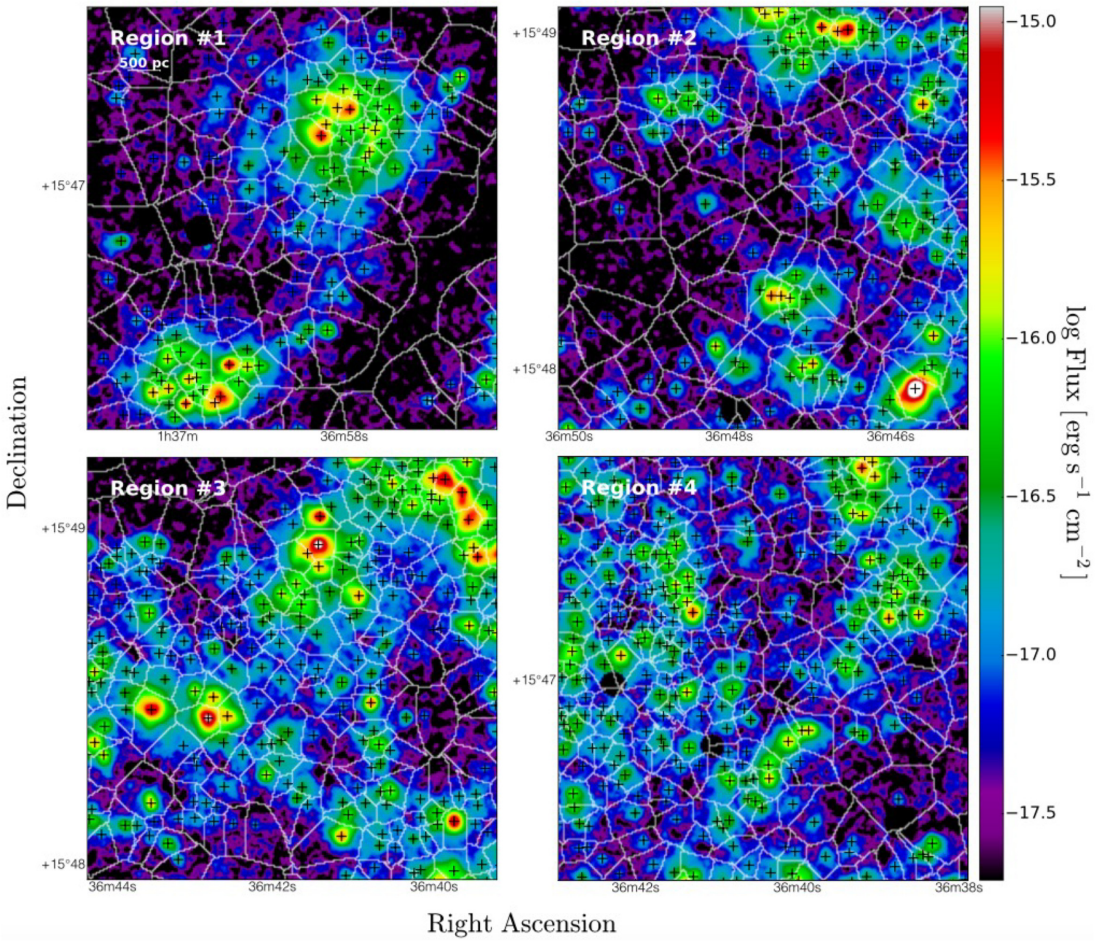

Figure 7. Examples of ionizing sources and their zone of influence in NGC 628 drawn over the Hα + Hβ + [O III]$\lambda\lambda$4959,5007 continuum-subtracted image from Rousseau-Nepton et al. (2018). The centroid position of each emission peak detected is identified with a cross. The white contours define the zones of influence surrounding the emission peaks.

with Hα, 84 per cent were also detected in [N II]λ6583, 91 per cent in [S II]$\lambda\lambda$6716+6731, 63 per cent in [O III]λ5007, 84 per cent in Hβ, and 63 per cent in [O II]λ3727. Part of the lower detection of the [O II]λ3727 line is due to dust extinction, a total exposure time of 2.13 h (lower than that for SIGNALS), and the loss of reflectivity of the telescope primary mirror (only a few months before realuminizing). For [O III]λ5007, about 5 per cent of the regions were at a metallicity too high to be detected and, as mentioned earlier in this section, the other non-detected regions could be older than 5 Myr and/or they have a low ionization parameter. From the distance of NGC 628 to the closest target of the sample, the fraction of detected lines increases as more pixels are available to extract the spectra. NGC 628 is therefore a worst case scenario for the detection of the lines.

4.6.2 *Integrated spectra modelling*

Grids of models covering different physical properties from various photoionization codes (BOND, Vale Asari et al. 2016; 3MdB, Morisset et al. 2015; and MAPPINGS, Dopita & Sutherland 1995) will be compared to the SIGNALS' H II region integrated spectra. These grids are designed to study the effect of variations in the gas conditions on the integrated spectrum (region by region). Fig. 10 shows an example of the comparison of emission line ratios observed in NGC 628 (Rousseau-Nepton et al. 2018) with BOND.

Different models can account for variations in the SED of the source, the metallicity [O/H], and the relative abundances of elements (e.g. [N/O]). The accuracy of the comparison with models can be improved by using a set of regions for which the ionization sources have been observationally constrained, e.g. LEGUS (Calzetti et al. 2015; Grasha et al. 2015). LEGUS provides access to both individual stars (Sabbi et al. 2018) and stellar cluster catalogues (Adamo et al. 2017). It also contains a fairly complete census of the massive stars (down to 15 $M_\odot$) and very young clusters (down to 10^3 $M_\odot$). Thus, the combined data from SIGNALS and LEGUS will provide a better view of the H II region physics for a large fraction of our sample.

4.6.3 *Spatially resolved modelling*

When an H II region is resolved, spatial variations of the ratios as a function of the distance to the source of ionization are expected. This can be due to the varying photoionization conditions in the gas as the intensity and slope of the ionizing spectrum, temperature, and density change. Once integrated, the variations can be less apparent (e.g. [NII]/[OII] ratio; see figures on p. 37 of Rousseau-Nepton at al. (2018)).

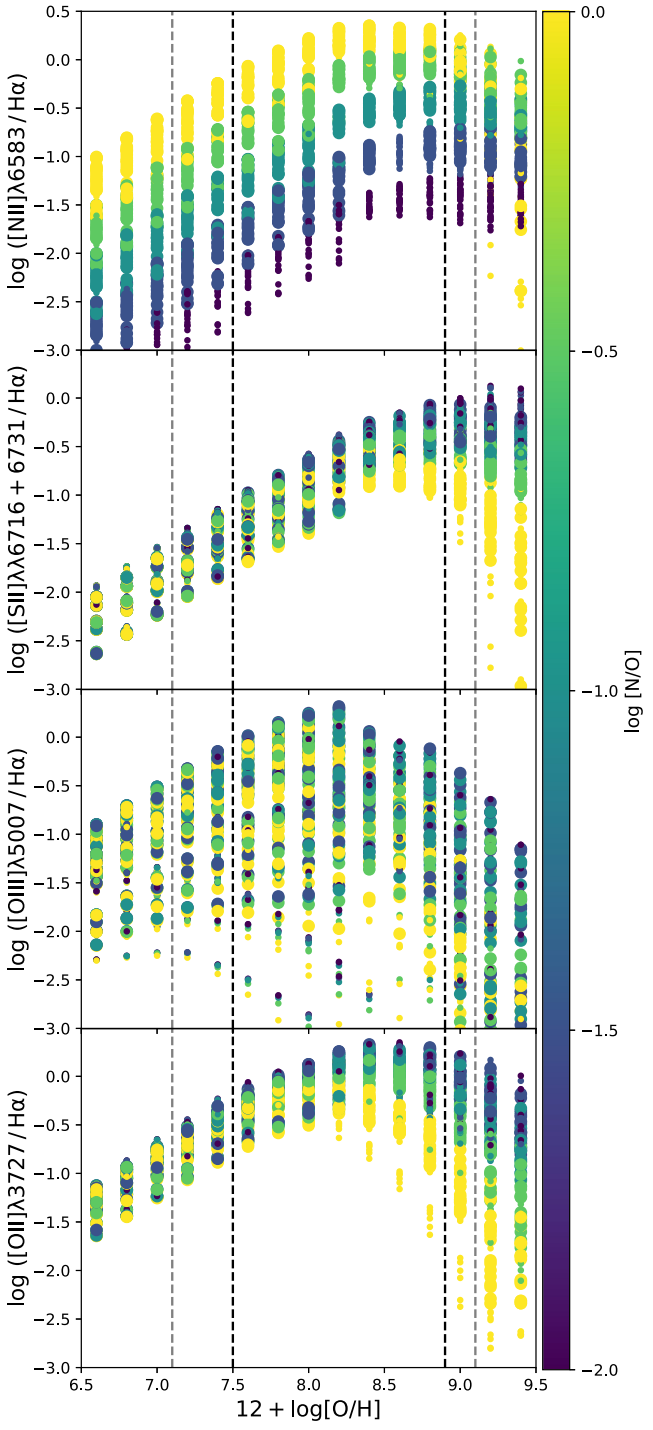

Figure 8. Prediction of several strong line ratios ([line]/Hα) of the CLOUDY photoionization code (extracted from the BOND grid of models on 3MdB). The colour scale represents the log[N/O] ratio for a given model. The smaller dots correspond to models representing less expected regions (log[N/O] < -1.5 or age >5.1 Myr or log[U] ≥ -3.55). The grey dashed vertical lines show the expected range of metallicity of the regions sampled and the black dashed vertical line shows the usual range of metallicity for most regions in the local Universe.

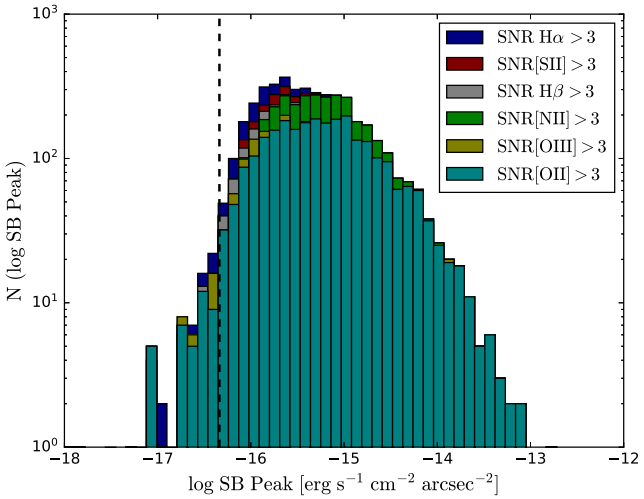

Figure 9. SB function of the H II regions in the commissioning data of NGC 628. The black dashed line shows the detection threshold of one element of resolution in Hα. The different colours represent selected subsets of regions for which there is a detection of different strong lines (see the legend). The few regions below the black dashed line are faint Hα regions detected from the combination of Hα, Hβ, and [O III]λ5007 used for the identification.

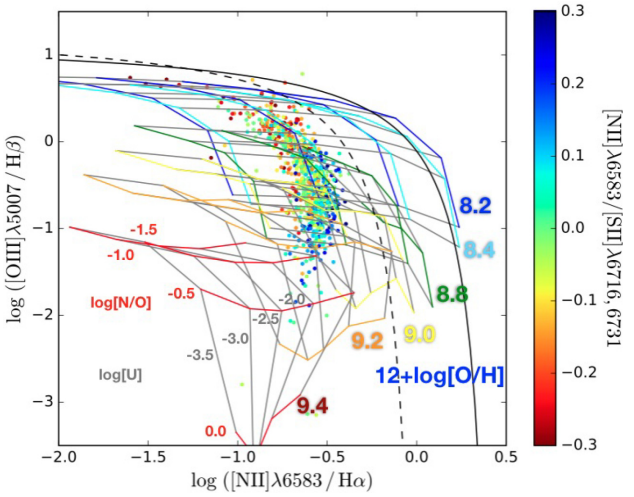

Figure 10. BPT diagram (Baldwin, Phillips & Terlevich 1981) of emission line regions identified in NGC 628 (from Rousseau-Nepton et al. 2018) along with a grid of models from BOND (Vale Asari et al. 2016) using the spectral energy distribution (SED) of a 3 Myr old stellar cluster with a Chabrier IMF (initial mass function) (Chabrier 2003). The colours of the grids indicate different metallicities (12 + log[O/H]). Horizontal lines have different values of log[N/O], as given in red for 12 + log[O/H] = 9.4, and vertical lines have different values of log[U], as given in grey for the same metallicity. The colour scale of the scattered observational points indicates the log([N II]/[S II]$\lambda\lambda$6716+6731) line ratio, which is known to be a good indicator of log[N/O] (Pérez-Montero et al. 2014). The limit between the H II regions and the transition regime (Kauffmann et al. 2003) is shown by the dashed curve, and the extent of the starburst domain (Kewley et al. 2001) is displayed by the continuous curve.

The 2D sampling of the line emission enables the use of multidimensional photoionization models to constrain gas properties (Wood et al. 2005, 2013; Weber, Pauldrach & Hoffmann 2015; Rahner et al. 2019). For each source identified, we establish a mean profile of the line ratios as a function of the distance to the ionization source (OB stars in the case of H II regions). These profiles along with the integrated flux of each line are needed to conduct a fair comparison with the models. Fig. 11 shows a comparison of four line ratios with a 2D projection of the pseudo-3D model extracted from PYCLOUDY (Morisset 2013).

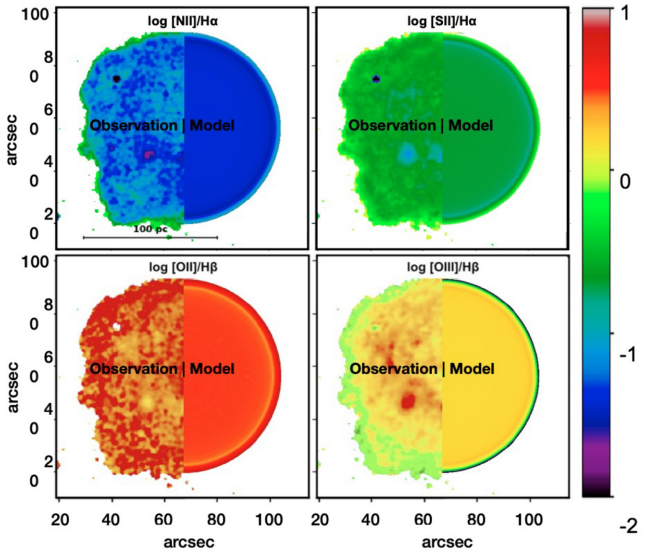

Figure 11. Comparison of a giant H II region observed with SITELLE in NGC 6822 with a 3D photoionization model projected on 2D images. The region is split into two for each panel: the left-hand side represents the observations, while the right-hand side is the model (a slice perpendicular to the line of sight that goes from the centre of the region to the outskirts). A pure 40 000 K Planck function was used as ionizing spectrum and abundances at 20 per cent of the solar value, except for S. The model was also for a thin shell of gas with $\log[U] = -2.6$.

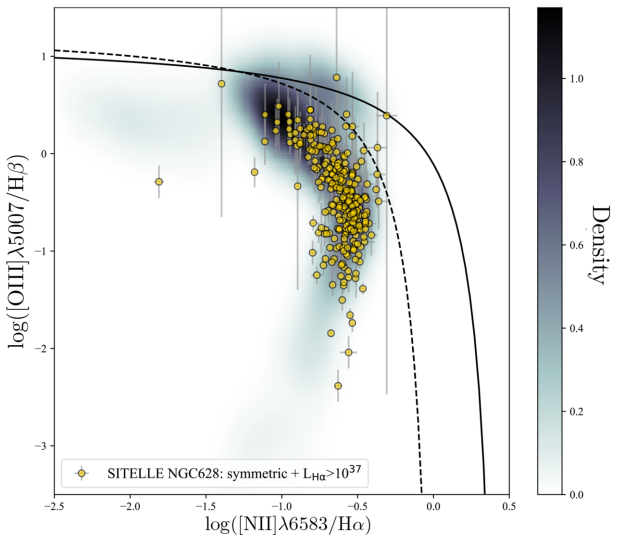

Figure 12. BPT diagram (Baldwin et al. 1981) of emission line regions identified in NGC 628 from Rousseau-Nepton et al. (2018), using circular regions only, along with simulations from CLOUDY using post-processing of evolutionary tracks from the WARPFIELD code (Pellegrini et al. 2019; Rahner et al. 2019). It combines a series of WARPFIELD runs with different cloud masses, densities, and ages. The colour coding indicates the relative number of model outputs used to produce a line ratio. See the caption of Fig. 10 for the curve definitions.

4.6.4 Modelling populations

In addition to the region-by-region analysis, a statistical approach is used to study populations of H II regions. Fig. 12 shows simulations of line ratios when combining photoionization models with evolutionary tracks of a population of star-forming clusters at solar metallicity. The emission measure predictor code WARPFIELD (Winds And Radiation Pressure: Feedback Induced Expansion, colLapse and Dissolution; Rahner et al. 2017, 2019; Pellegrini et al. 2019) was used to produce Fig. 12. WARPFIELD considers a semi-analytic model to describe the impact of mechanical and radiative feedback from a young massive cluster on its parental cloud. Its approach simultaneously and self-consistently calculates the structure and the expansion of shells driven by feedback from stellar winds, supernovae, and radiation pressure, while accounting for the deceleration of the shell due to gravity. The model has been used to investigate the conditions under which the different sources of feedback dominate and the amount of radiation that escapes through the shell. It was also used to derive the minimum star formation efficiency (SFE) for a large parameter space of clouds and clusters (Rahner et al. 2017). The same approach was used to explain the two stellar populations in NGC 2070 in the LMC, which hosts the younger cluster R136 in its centre (Rahner et al. 2018). Because this method is computationally very efficient, it will allow us to consider a large range of parameters. We are currently compiling a comprehensive data base where we vary the SFE, the cloud mass and density profile, and the metallicity of both the gas and the stars. Each model is currently being post-processed using CLOUDY to make detailed predictions for the time evolution of the line and continuum emission associated with the system. Using this code, we can build synthetic BPT-like diagrams for the one-to-one comparison with observational data, as shown in Fig. 12.

4.7 Feedback processes

Massive OB stars in H II regions are responsible not only for ionizing the surrounding gas but also for exerting direct radiation pressure on to this gas. They also return enriched material and mechanical energy through their stellar winds and supernova explosions to the ISM. While the efficiency of stellar winds involved in shaping an H II region bubble is still uncertain, it is possible that radiation pressure may play a dominant role at a younger age, while thermal pressure of the warm ionized gas may become more important at a later age (Lopez et al. 2014; Pellegrini et al. 2019). Also, the DIG can be observed near H II region boundaries. Recent works on the DIG have helped to quantify its emission in nearby galaxies (Lacerda et al. 2018; Moumen et al. 2019; Poetrodjojo et al. 2019) and photoionization models have been developed to trace back the SED of the source of ionization. Several sources of ionization might be responsible for the DIG: ionizing photons escaping H II regions that travel long distances (Ferguson et al. 1996; Zurita, Rozas & Beckman 2000; Oey et al. 2007; Haffner et al. 2009; Barnes et al. 2014; Howard, Pudritz & Harris 2016; Howard, Pudritz & Klessen 2017), a weak active galactic nucleus (AGN; Ho 2008; Davies et al. 2014), a generation of post-asymptotic giant branch stars (Binette et al. 1994; Flores-Fajardo et al. 2011), and fast shocks in the ISM (Allen et al. 2008; Hoffmann et al. 2012). Some studies have suggested that only OB stars could be responsible for most of the DIG emission (Domgorgen & Mathis 1994). Others have found that a mix of multiple sources could explain the observed line ratios in the DIG (Poetrodjojo et al. 2019; Weber et al. 2019)

Detailed numerical simulations predict that the fraction of escaping photons varies considerably over a few million year time-scale. Semi-analytic feedback models for the cloud dissolution (Rahner et al. 2017) have demonstrated that the SFE is linked to the ionizing escaping photons (i.e. a high SFE corresponds to a high fraction of escaping photons). Also, depending on the evolution phase of the H II region, the escaping photon fraction can change (Pellegrini

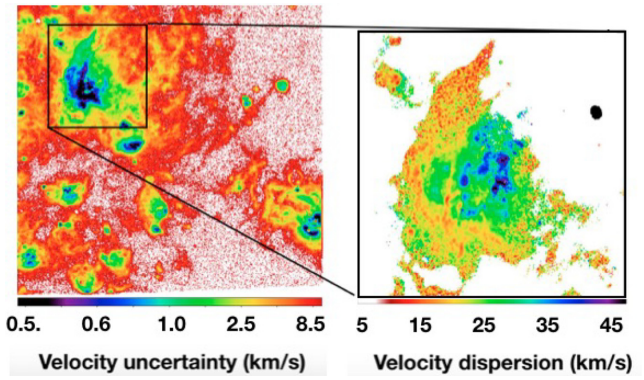

Figure 13. M33 Hα velocity uncertainties and dispersion for a small portion of the SITELLE FOV with $R = 3000$.

et al. 2019). SIGNALS will measure the DIG surrounding each H II region as shown in Rousseau-Nepton et al. (2018). By measuring the relative contribution of the H II regions to their surrounding DIG, we will get precise constraints on the fraction of radiation and hot gas escaping the regions that merges with the low-density ISM.

Our requirements for the study of feedback processes rely on (1) the spatial resolution to resolve regions, filaments, supernova remnants, etc.; (2) the depth of the observations to detect faint regions and DIG emission; and (3) the line ratios to track the ionizing front or its absence around H II regions along with the variation of chemical abundances in the gas. These requirements have already been met by the need to identify and characterize H II regions.

4.8 Kinematics and dynamics

The spectral resolution provided by SITELLE SN3 cubes for five lines simultaneously ($R = 5\,000$ for the Hα, [N II]$\lambda\lambda$6548,6583, and [S II]$\lambda\lambda$6717,6731 emission lines) will allow us to determine the line centroid (ORCS; see Section 2.2) with a precision of 0.1 to $\sim$10 km s^{-1} across the FOV. This will enable the detection of line broadening larger than 10 km s^{-1} in most H II regions (see Figs 3 and 13). It will also separate multiple components along the line of sight (Martin et al. 2016). Combined with the line ratio analysis discussed in the previous subsections, several aspects of the ionized gas dynamics will be probed: (1) shell expansion velocity in H II regions, from which their mass can be determined; (2) random and rotational motions as a function of location in the disc (e.g. spiral arms versus interarm regions and DIG); (3) azimuthal anisotropy of random motions in the disc plane; (4) kinematics and abundance patterns linked to the mixing mechanisms and abundance variations (Sánchez-Menguiano et al. 2016); (5) kinematics of the ionized gas compared; and (6) mass distribution models (Kam et al. 2017). In a few objects, the kinematics of the stellar halo should also be probed through the [O III]λ5007 emission line in PNe, allowing alternative derivations of rotation curves and mass profiles.

4.9 Impact of local environment

To investigate possible relations between star-forming regions and their environment, the following parameters will be studied: the local stellar density, local DIG background, local neutral gas density, local star formation rate and SFE, distances to the nearest regions, and location with regards to prominent galactic structures (bar, spiral arm, ring, AGN, etc.). The size, geometry, and total Hα luminosity will also be considered. A large variety of galaxies with different stellar populations and stellar densities can be found within the SIGNALS sample. Within each individual target, this distribution also changes dramatically from one area to another. While the diversity of targets adds complexity to the analysis, it makes the analysis robust because reliable subsamples can be used for specific purposes in addressing the main goals of the project.

5 DATA PRODUCTS

Fig. 14 summarizes the diverse processing steps presented in this paper, from the observational phase to the extraction of the physical parameters. The process differs between nearby (i.e. spatial resolution $\lesssim$15 pc) and more distant targets. The ORCS software can simultaneously or individually fit lines in each datacube while returning maps for each line, including the amplitude, FWHM, continuum height, flux, velocity, velocity dispersion, and their corresponding uncertainties. The H II regions identified with our procedure will be included in a catalogue that will contain the raw emission line measurements from the datacubes obtained after data processing and the stellar continuum subtraction. The median profile of each line will also be fitted as in Rousseau-Nepton et al. (2018); the fitting parameters will be provided in the catalogue. Extinction-corrected values will also be provided as explained in Section 4.4. The absolute position (right ascension and declination) of the centre of each region will be provided as well as the name of the host galaxies. Additional data products extracted from complementary data will be added to the catalogue when available (e.g. the mean μ_V around the regions, and the total HI and CO emission evaluated over the region radius).

Data products will be distributed to the collaborators and other communities from the SIGNALS website. The HDF5 files containing the reduced datacubes are available without any proprietary period from the programme 18BP41, 19AP41, ..., P41, etc., via the CADC website.[3] Data release of additional products following the analysis will be made available later from the SIGNALS website.

6 LEGACY VALUE

SIGNALS fills the gap between other galaxy surveys focusing on the local Universe, from the upcoming SDSS-V LVM survey to current surveys such as MAD, PHANGS, CALIFA, SAMI, MaNGA, etc. It will provide new, key insights into star formation and feedback mechanisms driving the evolution of the ISM in star-forming galaxies. By using multiple nebular lines, physical properties like abundances, ionization structures, and dynamics will be obtained as well as information on the impact of local environments on the star formation process.

The rich SIGNALS data set will be valuable for investigating other complementary astrophysical topics. Some possibilities include (1) planetary nebula abundance distributions and luminosity functions (Kreckel et al. 2017; Martin et al. 2018); (2) supernova remnant ionization conditions, occurrence, and feedback contribution (Moumen et al. 2019); (3) detection of background emission line objects (e.g. [O II] and Ly-α emitters); and (4) large-scale velocity mapping of galaxies. The SIGNALS collaboration team will make this data set available to the scientific community, and provide catalogues and diagnostic tools.

[3] http://www.cadc-ccda.hia-iha.nrc-cnrc.gc.ca/en/

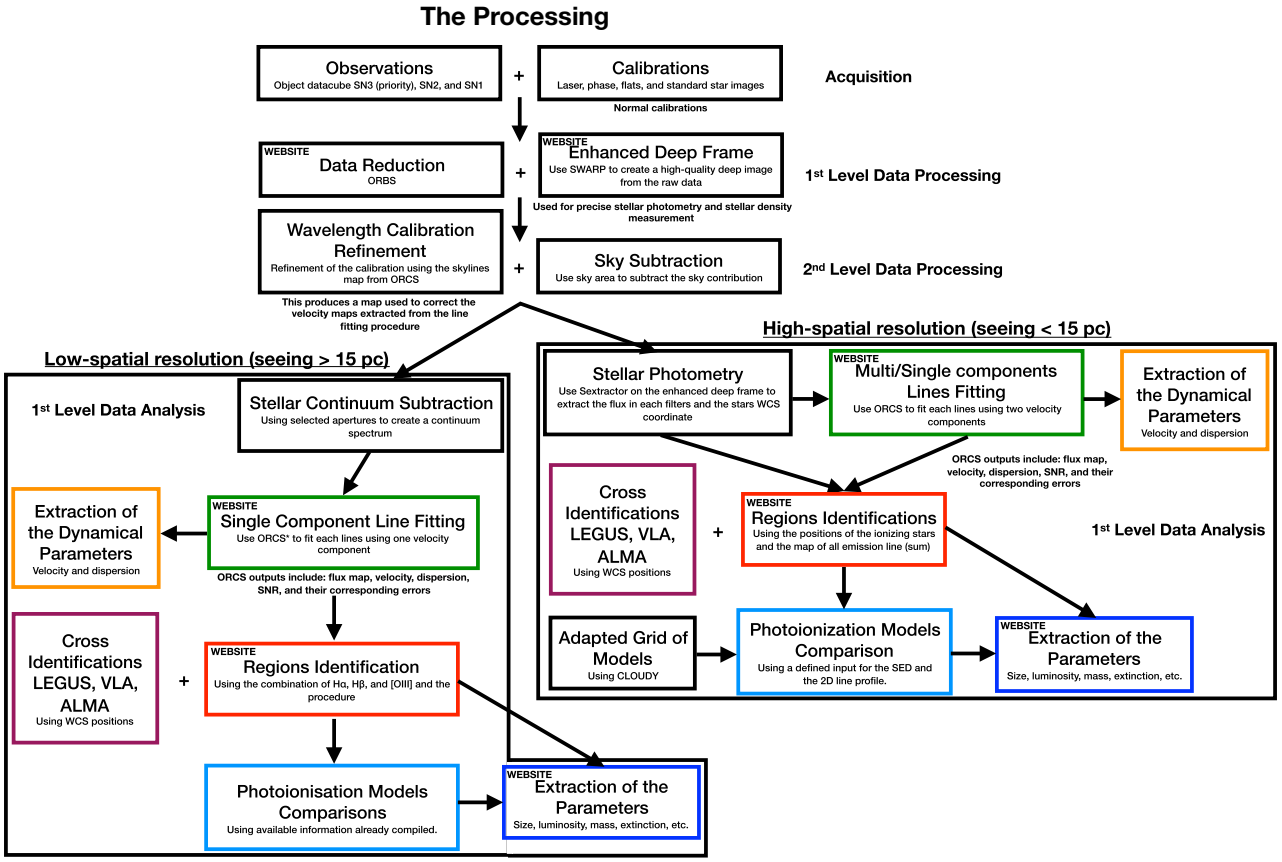

Figure 14. Organizational chart for the data processing. All items with the label WEBSITE will be accessible to everyone via our website (http://www.sign al-survey.org) once the collaboration team has analysed the data and published the different catalogues. Note that all observed datacubes are available at the Canadian Astronomical Data Center (CADC).

ACKNOWLEDGEMENTS

This research was based on observations obtained at the CFHT, which is operated from the summit of Mauna Kea by the National Research Council of Canada, the Institut National des Sciences de l'Univers of the Centre National de la Recherche Scientifique of France, and the University of Hawaii. The authors wish to recognize and acknowledge the very significant cultural role that the summit of Mauna Kea has always had within the indigenous Hawaiian community. The authors are most grateful to have the opportunity to conduct observations from this mountain. The observations were obtained with SITELLE, a joint project between Université Laval, ABB-Bomem, Université de Montréal, and the CFHT, with funding support from the Canada Foundation for Innovation (CFI), the National Sciences and Engineering Research Council of Canada (NSERC), Fonds de Recherche du Québec – Nature et Technologies (FRQNT), and CFHT. The collaboration is grateful to the FRQNT, CFHT, the Canada Research Chair programme, the NSERC, the Swedish Research Council (Vetenskapsrådet), the Swedish National Space Board (SNSB), the Royal Society and the Newton Fund via the award of a Royal Society–Newton Advanced Fellowship (NAF\R1\180403), FAPESC, CNPq, FAPESP (2014/11156-4), FAPESB (7916/2015), and CONACyT (CB2015-254132).

REFERENCES

Adamo A. et al., 2017, ApJ, 841, 131
Allen M. G., Groves B. A., Dopita M. A., Sutherland R. S., Kewley L. J., 2008, ApJS, 178, 20
Anderson L. D., Bania T. M., Balser D. S., Rood R. T., 2011, ApJS, 194, 32
Azimlu M., Marciniak R., Barmby P., 2011, AJ, 142, 139
Bacon R. et al., 2001, MNRAS, 326, 23
Bacon R. et al., 2010, in McLean I. S., Ramsay S. K., Takami H., eds, Proc. SPIE Conf. Ser. Vol. 7735, Ground-Based and Airborne Instrumentation for Astronomy III. SPIE, Bellingham, p. 773508
Baldwin J. A., Phillips M. M., Terlevich R., 1981, PASP, 93, 5
Barnes J. E., Wood K., Hill A. S., Haffner L. M., 2014, MNRAS, 440, 3027
Berg D. A., Skillman E. D., Croxall K. V., Pogge R. W., Moustakas J., Johnson-Groh M., 2015, ApJ, 806, 16
Binette L., Magris C. G., Stasińska G., Bruzual A. G., 1994, A&A, 292, 13
Blanc G. A. et al., 2013, AJ, 145, 138
Brousseau D., Thibault S., Fortin-Boivin S., Zhang H., Vallée P., Auger H., Drissen L., 2014, in Ramsay S. K., McLean I. S., Takami H., eds, Proc. SPIE Conf. Ser. Vol. 9147, Ground-Based and Airborne Instrumentation for Astronomy V. SPIE, Bellingham, p. 91473Z
Bryant J. J. et al., 2012, in McLean I. S., Ramsay S. K., Takami H., eds, Proc. SPIE Conf. Ser. Vol. 8446, Ground-Based and Airborne Instrumentation for Astronomy IV. SPIE, Bellingham, p. 84460X
Bundy K. et al., 2015, ApJ, 798, 7
Calzetti D. et al., 2015, AJ, 149, 51
Cardelli J. A., Clayton G. C., Mathis J. S., 1989, ApJ, 345, 245
Chabrier G., 2003, PASP, 115, 763
Chemin L. et al., 2006, MNRAS, 366, 812
Corwin H. G., Jr., Buta R. J., de Vaucouleurs G., 1994, AJ, 108, 2128
Croxall K. V., Pogge R. W., Berg D. A., Skillman E. D., Moustakas J., 2015, ApJ, 808, 42

Croxall K. V., Pogge R. W., Berg D. A., Skillman E. D., Moustakas J., 2016, ApJ, 830, 4
Daigle O., Carignan C., Amram P., Hernandez O., Chemin L., Balkowski C., Kennicutt R., 2006, MNRAS, 367, 469
Davies R. L., Rich J. A., Kewley L. J., Dopita M. A., 2014, MNRAS, 439, 3835
Domgorgen H., Mathis J. S., 1994, ApJ, 428, 647
Dopita M. A., Sutherland R. S., 1995, ApJ, 455, 468
Drissen L. et al., 2019, MNRAS, 485, 3930
Drory N. et al., 2015, AJ, 149, 77
Epinat B. et al., 2008, MNRAS, 388, 500
Erroz-Ferrer S. et al., 2019, MNRAS, 484, 5009
Ferguson A. M. N., Wyse R. F. G., Gallagher J. S., III, Hunter D. A., 1996, AJ, 111, 2265
Ferland G. J., Korista K. T., Verner D. A., Ferguson J. W., Kingdon J. B., Verner E. M., 1998, PASP, 110, 761
Flores-Fajardo N., Morisset C., Stasińska G., Binette L., 2011, MNRAS, 415, 2182
Garrido O., Marcelin M., Amram P., Boulesteix J., 2002, A&A, 387, 821
Grasha K. et al., 2015, ApJ, 815, 93
Haffner L. M. et al., 2009, Rev. Mod. Phys., 81, 969
Hernandez O., Gach J.-L., Carignan C., Boulesteix J., 2003, in Iye M., Moorwood A. F. M., eds, Proc. SPIE Conf. Ser. Vol. 4841, Instrument Design and Performance for Optical/Infrared Ground-Based Telescopes. SPIE, Bellingham, p. 1472
Hernández-Martínez L., Peña M., Carigi L., García-Rojas J., 2009, A&A, 505, 1027
Hill G. J. et al., 2008, in McLean I. S., Casali M. M., eds, Proc. SPIE Conf. Ser. Vol. 7014, Ground-Based and Airborne Instrumentation for Astronomy II. SPIE, Bellingham, p. 701470
Ho I.-T. et al., 2014, MNRAS, 444, 3894
Ho L. C., 2008, ARA&A, 46, 475
Hoffmann T. L., Lieb S., Pauldrach A. W. A., Lesch H., Hultzsch P. J. N., Birk G. T., 2012, A&A, 544, A57
Houck J. R. et al., 2004, ApJS, 154, 18
Howard C. S., Pudritz R. E., Harris W. E., 2016, MNRAS, 461, 2953
Howard C., Pudritz R., Klessen R., 2017, ApJ, 834, 40
Hunter D. A., Hoffman L., 1999, AJ, 117, 2789
Kam S. Z., Carignan C., Chemin L., Foster T., Elson E., Jarrett T. H., 2017, AJ, 154, 41
Kauffmann G. et al., 2003, MNRAS, 346, 1055
Kewley L. J., Dopita M. A., 2002, ApJS, 142, 35
Kewley L. J., Dopita M. A., Sutherland R. S., Heisler C. A., Trevena J., 2001, ApJ, 556, 121
Kniazev A. Y., Grebel E. K., Pustilnik S. A., Pramskij A. G., Zucker D. B., 2005, AJ, 130, 1558
Kollmeier J. A. et al., 2017, preprint (arXiv:1711.03234)
Konstantopoulos I. et al., 2013, Am. Astron. Soc. Meeting Abstracts #221, p. 215.01
Kreckel K., Groves B., Bigiel F., Blanc G. A., Kruijssen J. M. D., Hughes A., Schruba A., Schinnerer E., 2017, ApJ, 834, 174
Lacerda E. A. D. et al., 2018, MNRAS, 474, 3727
Laurent F., Henault F., Renault E., Bacon R., Dubois J.-P., 2006, PASP, 118, 1564
Lopez L. A., Krumholz M. R., Bolatto A. D., Prochaska J. X., Ramirez-Ruiz E., Castro D., 2014, ApJ, 795, 121
McLeod A. F., Dale J. E., Ginsburg A., Ercolano B., Gritschneder M., Ramsay S., Testi L., 2015, MNRAS, 450, 1057
Martin T., Drissen L., 2017, preprint (arXiv:1706.03230)
Martin T., Drissen L., Joncas G., 2015, in Taylor A. R., Rosolowsky E., eds, ASP Conf. Ser. Vol. 495, Astronomical Data Analysis Software and Systems XXIV (ADASS XXIV). Astron. Soc. Pac., San Francisco, p. 327
Martin T. B., Prunet S., Drissen L., 2016, MNRAS, 463, 4223
Martin T. B., Drissen L., Melchior A.-L., 2018, MNRAS, 473, 4130
Morisset C., 2013, Astrophysics Source Code Library, record ascl:1304.020
Morisset C., Delgado-Inglada G., Flores-Fajardo N., 2015, Rev. Mex. Astron. Astrofis., 51, 103
Morisset C. et al., 2016, A&A, 594, A37
Moumen I., Robert C., Devost D., Martin R. P., Rousseau-Nepton L., Drissen L., Martin T., 2019, MNRAS, 488, 803
Moustakas J., Kennicutt Robert C. J., Tremonti C. A., Dale D. A., Smith J.-D. T., Calzetti D., 2010, ApJS, 190, 233
Oey M. S. et al., 2007, ApJ, 661, 801
Pellegrini E. W., Oey M. S., Winkler P. F., Points S. D., Smith R. C., Jaskot A. E., Zastrow J., 2012, ApJ, 755, 40
Pellegrini E. W., Reissl S., Rahner D., Klessen R. S., Glover S. C. O., Pakmor R., Herrera-Camus R., Grand R. J. J., 2019, preprint (arXiv:1905.04158)
Pérez-Montero E., Monreal-Ibero A., Relaño M., Vílchez J. M., Kehrig C., Morisset C., 2014, A&A, 566, A12
Pilyugin L. S., Contini T., Vílchez J. M., 2004, A&A, 423, 427
Pilyugin L. S., Grebel E. K., Kniazev A. Y., 2014, AJ, 147, 131
Pilyugin L. S., Grebel E. K., Zinchenko I. A., 2015, MNRAS, 450, 3254
Poetrodjojo H., D'Agostino J. J., Groves B., Kewley L., Ho I. T., Rich J., Madore B. F., Seibert M., 2019, MNRAS, 487, 79
Rahner D., Pellegrini E. W., Glover S. C. O., Klessen R. S., 2017, MNRAS, 470, 4453
Rahner D., Pellegrini E. W., Glover S. C. O., Klessen R. S., 2018, MNRAS, 473, L11
Rahner D., Pellegrini E. W., Glover S. C. O., Klessen R. S., 2019, MNRAS, 483, 2547
Rosales-Ortega F. F., Díaz A. I., Kennicutt R. C., Sánchez S. F., 2011, MNRAS, 415, 2439
Rosolowsky E. et al., 2019, Am. Astron. Soc. Meeting Abstracts #233, p. 450.01
Roth M. M. et al., 2005, PASP, 117, 620
Roth M. M. et al., 2018, A&A, 618, A3
Rousseau-Nepton L., Robert C., Martin R. P., Drissen L., Martin T., 2018, MNRAS, 477, 4152
Sabbi E. et al., 2018, ApJS, 235, 23
Sakai S., Ferrarese L., Kennicutt Robert C. J., Saha A., 2004, ApJ, 608, 42
Sánchez S. F., Cardiel N., Verheijen M. A. W., Martín-Gordón D., Vilchez J. M., Alves J., 2007, A&A, 465, 207
Sánchez S. F. et al., 2012, A&A, 538, A8
Sánchez-Menguiano L. et al., 2016, ApJ, 830, L40
Skillman E. D., Terlevich R., Melnick J., 1989, MNRAS, 240, 563
Skillman E. D., Bomans D. J., Kobulnicky H. A., 1997, ApJ, 474, 205
Smith C., Leiton R., Pizarro S., 2000, in Alloin D., Olsen K., Galaz G., eds, ASP Conf. Ser. Vol. 221, Stars, Gas and Dust in Galaxies: Exploring the Links. Astron. Soc. Pac., San Francisco, p. 83
The Nearby Supernova Factory et al., 2013, A&A, 549, A8
Tremblin P. et al., 2014, A&A, 568, A4
Vale Asari N., Stasińska G., Morisset C., Cid Fernandes R., 2016, MNRAS, 460, 1739
van Zee L., Skillman E. D., Haynes M. P., 2006, ApJ, 637, 269
Weber J. A., Pauldrach A. W. A., Hoffmann T. L., 2015, A&A, 583, A63
Weber J. A., Pauldrach A. W. A., Hoffmann T. L., 2019, A&A, 622, A115
Weilbacher P. M. et al., 2015, A&A, 582, A114
Wood K., Haffner L. M., Reynolds R. J., Mathis J. S., Madsen G., 2005, ApJ, 633, 295
Wood K., Barnes J. E., Ercolano B., Haffner L. M., Reynolds R. J., Dale J., 2013, ApJ, 770, 152
Yan R., MaNGA Team 2016, Am. Astron. Soc. Meeting Abstracts #227, p. 312.02
Zurita A., Rozas M., Beckman J. E., 2000, A&A, 363, 9

APPENDIX A: SAMPLE TABLE

Table A1. List of targets for SIGNALS.

ID (1)	RA (2)	Dec. (3)	Morphology (4)	D (5)	m (6)	M (7)	a (8)	b (9)	i (10)	Z (11)	Ref_Z (12)	PHANGS (13)	LEGUS (14)	*HST* (15)	*GALEX* (16)	*Spitzer* (17)	CO (18)	VLA (19)
WLM	00h01m58.16s	−15d27m39.3s	IB(s)m	1.03	11.03	− 14.93	11.5	4	70	7.74	2				x	x		x
M31	00h42m44.35s	+41d16m08.6s	SA(s)b	0.78	4.36	− 21.20	190	60	71	8.72	1			x	x		x	x
NGC 247	00h47m08.55s	−20d45m37.4s	SAB(s)d	3.27	9.86	− 19.24	21.4	6.9	71					x	x	x		x
NGC 337A	01h01m33.90s	−07d35m17.7s	SAB(s)dm	8.13	12.7B	− 18.67	5.9	4.5	41						x	x		
IC 1613	01h04m47.79s	+02d07m04.0s	IB(s)m	0.72	9.88	− 14.55	16.2	14.5	27	7.86	2				x	x		x
M33	01h33m50.89s	+30d39m36.8s	SA(s)cd	0.87	6.27	− 18.94	70.8	41.7	54	8.48	1			x	x	x		x
NGC 628	01h36m41.75s	+15d47m01.2s	SA(s)c	8.985	9.95	− 20.68	10.5	9.5	24	8.78	1		x	x	x	x	x	x
IC 1727	01h47m29.89s	+27d20m00.1s	SB(s)m	6.96	12.07	− 18.32	6.9	3.1	63						x	x		x
NGC 672	01h47m54.52s	+27d25m58.0s	SB(s)cd	7.32	11.47	− 18.94	7.2	2.6	69					x	x	x		x
NGC 925	02h27m16.88s	+33d34m45.0s	SAB(s)d	7.85	10.69	− 20.05	10.5	5.9	56	8.48	1			x	x	x	x	x
NGC 1042	02h40m23.97s	−08d26m00.8s	SAB(rs)cd	7.85	11.5B	− 17.51	4.7	3.6	39						x	x		x
M77	02h42m40.71s	−00d00m47.8s	(R)SA(rs)b	10.58	9.61	− 20.58	7.1	6	32	8.64	1			x	x	x	x	x
NGC 1058	02h43m30.00s	+37d20m28.8s	SA(rs)c	5.2	11.2V	− 18.89	3	2.8	24	8.64	1							
NGC 1073	02h43m40.52s	+01d22m34.0s	SB(rs)c	7.37	11.47	− 19.87	4.9	4.5	24							x		x
NGC 1156	02h59m42.30s	+25d14m16.2s	IB(s)m	6.09	12.32	− 18.56	3.3	2.5	42	8.16	9			x	x		x	x
NGC 2283	06h45m52.69s	−18d12m37.2s	SB(s)cd	9.92	12.93	− 18.93	3.6	2.8	41			x						
NGC 2903	09h32m10.11s	+21d30m03.0s	SAB(rs)bc	7.99	9.68	− 21.02	12.6	6	61	8.82	1	x		x	x	x	x	x
Sextans B	10h00m00.10s	+05d19m56.0s	IB(s)m	1.55	11.85	− 14.39	5.1	3.5	46	7.5	3				x	x		x
Sextans A	10h11m00.80s	−04d41m34.0s	IBm	1.43	11.86	− 13.56	5.9	4.9	34	7.53	3				x	x		x
UGC 5829	10h42m41.91s	+34d26m56.0s	Im	8	13.73	− 16.73	4.7	4.2	27						x	x		
NGC 3344	10h43m31.15s	+24d55m20.0s	(R)SAB(r)bc	12.44	10.45	− 19.64	7.1	6.5	24	8.72	1		x	x	x	x	x	x
M95	10h43m57.70s	+11d42m13.7s	SB(r)b	9.97	11.4G	− 19.84	3.07	2.86	47	8.82	1	x	x	x	x	x	x	x
NGC 3377A	10h47m22.30s	+14d04m10.0s	SAB(s)m	7.44	14.22	− 15.64	2.2	2.1	17									
M66	11h20m14.96s	+12d59m29.5s	SAB(s)b	9.59	9.65	− 21.21	9.1	4.2	63	8.34	4	x	x	x	x	x	x	x
NGC 3631	11h21m02.87s	+53d10m10.4s	SA(s)c	10.32	11.01	− 21.02	5	4.8	17	8.71	1					x	x	x
NGC 3642	11h22m17.90s	+59d04m28.0s	SA(r)bc	8.378	12.6	− 20.57	1.76	1.53	34									x
NGC 4027	11h59m30.17s	−19d15m54.8s	SB(s)dm	12.24	11.66	− 20.66	3.2	2.4	41							x		x
NGC 4151	12h10m32.58s	+39d24m2.6s	(R')SAB(rs)ab	9.92	11.5	− 17.30	6.3	4.5	45					x		x	x	x
NGC 4214	12h15m39.17s	+36d19m36.8s	IAB(s)m	2.98	10.24	− 17.46	8.5	6.6	39	8.2	9			x	x	x	x	x
NGC 4242	12h17m30.18s	+45d37m09.5s	SAB(s)dm	6.4	11.2B	− 17.46	5	3.8	41				x	x	x	x		x
M106	12h18m57.50s	+47d18m14.3s	SAB(s)bc	7.28	8.41V	− 20.94	18.6	7.2	67	8.54	1		x	x	x	x	x	x
NGC 4314	12h22m31.82s	+29d53m45.2s	SB(rs)a	9.7	11.43	− 19.90	4.2	3.7	27									
NGC 4395	12h25m48.86s	+33d32m48.9s	SA(s)m:	4.23	10.64	− 18.51	13.2	11	34	8.32	9		x	x	x	x		x
NGC 4449	12h28m11.10s	+44d05m37.1s	IBm	3.86	9.99	− 19.17	6.2	4.4	45	8.26	9		x	x	x	x		x
UGC 7608	12h28m44.20s	+43d13m26.9s	Im	8.25	13.67	− 16.76	3.4	3.3	12						x	x		
NGC 4490	12h30m36.24s	+41d38m38.0s	SB(s)d pec	6.21	10.22	− 21.49	6.3	3.1	61	8.29	1		x	x	x	x	x	x
UGC 7698	12h32m54.39s	+31d32m28.0s	Im	4.21	13.0	− 15.70	6.5	4.5	46	8.2	7				x	x		x
NGC 4618	12h41m32.85s	+41d09m02.8s	SB(rs)m	7.24	11.22	− 19.44	4.2	3.4	36						x	x		x
M94	12h50m53.06s	+41d07m13.6s	(R)SA(r)ab	5.11	8.99	− 19.67	11.2	9.1	36	8.57	1			x	x		x	x
IC 4182	13h05m49.54s	+37d36m17.6s	SA(s)m	4.21	13.0	− 15.74	6	5.5	24						x	x		
M63	13h15m49.33s	+42d01m45.4s	SA(rs)bc	7.72	9.31	− 20.89	12.6	7.2	55	8.87	1			x	x	x	x	x

Table A1 – *continued*

ID (1)	RA (2)	Dec. (3)	Morphology (4)	D (5)	m (6)	M (7)	a (8)	b (9)	i (10)	Z (11)	Ref_Z (12)	PHANGS (13)	LEGUS (14)	*HST* (15)	*GALEX* (16)	*Spitzer* (17)	CO (18)	VLA (19)
NGC 5068	13h18m54.80s	−21d02m21.0s	SAB(rs)cd	5.989	10.52	−18.54	7.2	6.3	29			x			x	x		x
NGC 5204	13h29m36.51s	+58d25m07.4s	SA(s)m	5.22	11.73	− 17.01	5	3	53						x	x		x
M51	13h29m52.71s	+47d11m42.6s	SA(s)bc pec	7.18	8.96	− 21.33	11.2	6.9	52	8.88	1		x	x	x	x	x	x
NGC 5247	13h38m03.04s	−17d53m02.5s	SA(s)bc	9.35	10.5B	− 21.31	5.6	4.9	29					x		x	x	x
M101	14h03m12.54s	+54d20m56.2s	SAB(rs)cd	6.85	8.31	− 20.97	28.8	26.9	21	8.71	1		x	x	x	x	x	x
NGC 5474	14h05m01.61s	+53d39m44.0s	SA(s)cd pec	4.34	11.28	− 18.07	4.8	4.3	27	8.19	1		x	x	x	x	x	x
NGC 5585	14h19m48.20s	+56d43m44.6s	SAB(s)d	7.37	11.2	− 18.71	5.8	3.7	50					x	x	x		x
UGC 10310	16h16m18.35s	+47d02m47.1s	SB(s)m	7.91	13.58	− 17.41	2.8	2.2	37							x		
NGC 6814	19h42m40.64s	−10d19m24.6s	SAB(rs)bc	11.75	12.06	− 21.57	3	2.8	21									x
NGC 6822	19h44m57.74s	−14d48m12.4s	IB(s)m	0.52	9.31	− 15.02	15.5	13.5	29	8.06	8			x	x	x		x
NGC 6946	20h34m52.30s	+60d09m14.0s	SAB(rs)cd	5.545	8.23	−20.90	11.5	9.8	32					x		x	x	x
UGC 12082	22h34m10.82s	+32d51m37.8s	Sm	9.79	14.1	− 17.14	2.6	2.2	32									
UGC 12632	23h29m58.67s	+40d59m24.8s	Sm	9.44	12.78	− 17.69	4.5	3.7	34									

Notes. (1) Identification of the galaxy.
(2) Right ascension (2000).
(3) Declination (2000).
(4) Morphology from the Third Reference Catalogue of Bright Galaxies (RC3; Corwin, Buta & de Vaucouleurs 1994).
(5) Mean distance (Mpc) from NED.
(6) Apparent magnitude (mag) (note *B*, G, or *V* if the only one available).
(7) Absolute magnitude (mag).
(8) Major axis size (arcmin).
(9) Minor axis size (arcmin).
(10) Inclination (deg) from the RC3.
(11) Estimated global metallicity (see item 12).
(12) Reference for the global metallicity estimate: (1) Pilyugin, Grebel & Kniazev (2014); (2) Sakai et al. (2004); (3) Kniazev et al. (2005); (4) Moustakas et al. (2010); (7) Hunter & Hoffman (1999); (8) Hernández-Martínez et al. (2009); (9) Pilyugin, Grebel & Zinchenko (2015); (10) Skillman, Terlevich & Melnick (1989); (11) Skillman, Bomans & Kobulnicky (1997); (12) van Zee, Skillman & Haynes (2006).
(13) Target included in the PHANGS survey (x).
(14) Target included in the LEGUS survey (x).
(15) Target with observations available from *HST* (x).
(16) Target with observations available from *GALEX* (x).
(17) Target with observations available from *Spitzer* (x).
(18) Target with CO observations available (x).
(19) Target with HI observations available from the Very Large Array (x).

[1]*Canada–France–Hawaii Telescope, Kamuela, HI, 96743, USA*
[2]*Department of Physics and Astronomy, University of Hawaii at Hilo, Hilo, HI, 96720-4091, USA*
[3]*Département de physique, de génie physique et d'optique and Centre de Recherche en Astrophysique du Québec, Université Laval, Québec City, QC, G1V 0A6, Canada*
[4]*Aix Marseille University, CNRS, CNES, LAM, Marseille, 13013, France*
[5]*Department of Astronomy, The Oskar Klein Centre, Stockholm University, Stockholm, 114 19, Sweden*
[6]*Instituto de Astronomia, Universidad Nacional Autonoma de Mexico, Apdo. postal 70-264, Ciudad Universitaria, Mexico City, 04510, Mexico*
[7]*Department of Physics and Astronomy, University of Western Ontario, London, ON, N6A 3K7, Canada*
[8]*Institute for Astronomy, University of Hawaii, Honolulu, HI, 96822-1897, USA*
[9]*Sub-department of Astrophysics, University of Oxford, Denys Wilkinson Building, Keble Road, Oxford, OX1 2JD, UK*
[10]*Centro de Astronomía, Universidad de Antofagasta, Avda. U. de Antofagasta 02800, Antofagasta, Chile*
[11]*Departamento de Física – CFM, Universidade Federal de Santa Catarina, Florianópolis, Santa Catarina, 88040-900, Brazil*
[12]*LERMA, Observatoire de Paris, PSL Research University, CNRS, Université de Sorbonne, UPMC, Paris, 75014, France*
[13]*Collège de France, 11 Pl Marcelin Berthelot, Paris, 75005, France*
[14]*Instituto de Astrofísica de Andalucía – CSIC, Granada, 18008, Spain*
[15]*Institute of Astronomy, The University of Tokyo, Tokyo, 113-8654, Japan*
[16]*Universität Heidelberg, Zentrum für Astronomie, Heidelberg, 69117, Germany*
[17]*Observatoire de Genève, Université de Genève, Sauverny, 1290, Switzerland*
[18]*Instituto de Astronomia, Universidad Nacional Autonoma de Mexico, Ensenada, B.C., 22860, Mexico*
[19]*Max Planck Institute for Astronomy, Heidelberg, 69117, Germany*
[20]*Research School of Astronomy and Astrophysics, Australian National University, Canberra, ACT 0200, Australia*
[21]*ARC Centre of Excellence for All Sky Astrophysics in 3 Dimensions, ACT 2609, Australia*
[22]*University of Victoria, Victoria, BC, V9P 5C2, Canada*
[23]*NRC Herzberg Institute of Astrophysics, Victoria, BC, V8X 4M6, Canada*
[24]*Département de Physique, Université de Montréal, Montréal, QC, H3C 3J7, Canada*
[25]*Estación Experimental de Zonas Áridas, Almería, 04120, Spain*
[26]*Observatoire d'Astrophysique de l'Université de Ouagadougou, Ouagadougou, 03 BP 7021, Burkina Faso*
[27]*Department of Astronomy, University of Cape Town, Cape Town, 770, South Africa*
[28]*Steward Observatory, University of Arizona, Tucson, AZ, 85719, USA*
[29]*Institute for Astronomy, Astrophysics, Space Applications & Remote Sensing, National Observatory of Athens, P. Penteli, Athens, 15236, Greece*
[30]*Department of Astronomy & Astrophysics, University of Toronto, Toronto, ON, M5S 3H8, Canada*
[31]*Department of Physics, University of Warwick, Coventry, CV4 7AL, UK*
[32]*Department of Astronomy, University of California – Berkeley, Berkeley, CA, 94720-5800, USA*
[33]*Department of Physics and Astronomy, Texas Tech University, PO Box 41051, Lubbock, TX, 79409, USA*
[34]*Departamento de Investigacióon Básica, CIEMAT, Madrid, 28040, Spain*
[35]*Department of Astronomy, School of Science, The University of Tokyo, Tokyo, 113-8654, Japan*
[36]*Institute of Astronomy, National Tsing Hua University, Hsinchu, 300, Taiwan*
[37]*Academia Sinica, Institute of Astronomy & Astrophysics, Taipei, 10617, Taiwan*
[38]*Indian Institute of Astrophysics, Bangalore, Karnataka, 560034, India*
[39]*Department of Physics and Astronomy, State University of New York at Geneseo, Geneseo, NY, 14454, USA*
[40]*Departamento de Física Teórica y del Cosmos, Facultad de Ciencias (Edificio Mecenas), Universidad de Granada, Granada, 18071, Spain*
[41]*Instituto Universitario Carlos I de Física Teórica y Computacional, Universidad de Granada, Granada, 18071, Spain*
[42]*Institute for Astronomy, University of Hawaii, Honolulu, HI, 96822-1897, USA*
[43]*Laboratório de Astrofísica Teórica e Observacional, Universidade Estadual de Santa Cruz, Ilhéus, Bahia, 45650-000, Brazil*
[44]*Instituto de Astrofísica de Canarias, Tenerife, 38205, Spain*
[45]*Departamento de Astrofísica, Universidad de La Laguna, Tenerife, 38205, Spain*
[46]*Department of Physics and Space Science, Royal Military College of Canada, Kingston, ON, K7K 7B4, Canada*
[47]*LUTH, CNRS, Observatoire de Paris, PSL University, Meudon, 92190, France*
[48]*School of Physics and Astronomy, University of St Andrews, North Haugh, St Andrews KY16 9SS, UK*
[49]*Royal Society–Newton Advanced Fellowship*

This paper has been typeset from a TEX/LATEX file prepared by the author.